Eidgenössische Technische Hochschule Zürich
Swiss Federal Institute of Technology Zurich

INVESTIGATING THE SUPPRESSION OF EXTERNAL SOURCES OF DECOHERENCE IN TRANSMON QUBITS

Michael Peterer

Master Thesis
Institute for Solid State Physics
ETH Zurich

Supervisor: Dr. Arkady Fedorov
Handed in to: Prof. Dr. Andreas Wallraff

Zurich, June 17, 2012

To Karen, an amazing girl.

Abstract

Circuit quantum electrodynamics using superconducting qubits as elements of quantum information is a promising architecture to realize a quantum computer. The great experimental challenge to date is achieving the long qubit coherence times necessary for quantum computing. Like all open quantum systems, the qubits are however subject to various dissipation and dephasing effects which destroy its quantum coherence. One source of decoherence is believed to be the tunneling of quasiparticles generated by the external radiation present in the cryogenic apparatus. To suppress this radiation we embedded the sample and its holder in an absorptive medium and then compared the relaxation and dephasing times at various qubit transition frequencies before and after the embedding. Similar measurements without embedding were then performed on a new sample with a transmon having an increased gap between its finger capacitors. We observed an improvement in coherence times by a factor of 2-3 times and a clear dependance on the qubit frequency. Finally a possible model fitting this dependency was developed and compared to recent experiments, suggesting that it is 1/f noise from two-level fluctuators that could be affecting the coherence of our qubits at the current stage.

Contents

Chapter 1

Introduction

Realizing a quantum computer has become an active area of research in the past few years, not only because of its enormous economical interests, but also because it would allow for quantum simulation which would boost the development of the natural and engineering sciences. The arrival of the quantum computer is a natural consequence of the fact that the miniaturization of classical computer hardware components cannot continue forever, because at some point quantum mechanical effects start taking effect. Current technology will have reached this limit for the transistor sizes in a few years, namely at the scale of a few nanometers, and then we will be forced to embrace the quantum physics to continue the development of computers.

The idea of a quantum computer is to take advantage of the quantum coherence allowing for the two bit states 0 and 1 to be in any linear superposition, thereby forming a quantum bit (qubit). The fundamentally different nature of quantum information allows a processor to execute various quantum algorithms and perform quantum simulation. Up to date only a few quantum algorithms are known, but they have widespread important applications and they cannot be performed in reasonable times by even the most powerfull classical computer possibly imaginable. Such quantum algorithms can factorize large numbers exponentially faster than a classical computer (Shor's factoring algorithm [1]), which allow to crack common "public-key" cryptography in a short time, and can search large unsorted databases with much higher efficiency (Grover's search algorithm [2]). Moreover, a classical computer cannot simulate efficiently a many-particle quantum system (Richard Feynman [3]), even for just a few degrees of freedom. Simulating an entire molecule for example requires the ability to operate a very large number of degrees of freedom. A quantum computer could simulate it though with a number of qubits similar to the number of particles in the molecule. Just imagine the potential applications for the development of drugs in the pharmaceutical industry, as an example, if one can completely simulate entire molecules efficiently.

First implementations of quantum bits have already been realized in various physical systems: ion traps, NMR, quantum dots, superconducting qubits, nitrogen vacancy centers in diamonds, and more. Each approach has its advantages and drawbacks. One of the most promising are superconducting qubits, which are developed and studied at the Quantum Device Lab at ETH Zurich under the direction of Prof. Dr. Andreas Wallraff. The idea behind these devices is to implement cavity quantum electrodynamics (QED) with superconducting electrical circuits, leading to circuit QED. The qubits, called transmons, are based on Josephson junctions forming a Cooper Pair Box, and are capacitively coupled to a one-dimensional microwave transmission line resonator serving as a control and read-out channel.

One of the big challenges in building a quantum information processor is to suppress dissipation and dephasing processes which destroy the quantum coherence of the qubit. This decoherence is caused by interactions with the environment and by fluctuations and noise of the control parameters of the device. Significant effort worldwide is made to identify

the sources of decoherence and describe in detail the microscopic mechanisms leading to the energy relaxation and dephasing of the qubit state. Still little is known though as to exactly which processes currently limit the coherence times of superconducting qubits. This thesis presents an investigation to the possible suppression of a specific source of decoherence and it's effect on the decay rates of the transmons operated at ETH Zurich.

The first chapter introduces the general theory on qubits, the Josephson junction, the Cooper Pair Box, cavity and circuit QED and decoherence. Chapter 2 presents the measurement setup for an 8-port sample with three qubits and one resonator, and the motivation for suppressing external radiation from the dilution refrigerator. Chapter 3 describes how to embed the sampleholder into an microwave absorptive medium called Eccosorb. Chapter 4 presents the measurement results of the relaxation and dephasing times of our qubits before and after the embedding. Finally, chapter 5 introduces a new 16-port sample with four qubits and three cross resonators, and then presents measurement results for coherence times with these new slightly improved qubits.

Chapter 2

Theory

In this chapter, the basic theory on cavity and circuit quantum electrodynamics (QED) is introduced. The first section presents the quantum bit and its representation on the Bloch sphere, then the Josephson junction and how it allows to build an anharmonic two-level system, the Cooper Pair Box, and finally how it can be rendered charge-noise insensitive by operating it in the transmon regime. The second section introduces the Jaynes-Cummings Hamiltonian, then explains how the cavity QED can be realized in superconducting electrical circuits with a coplanar waveguide resonator, then how external drives allow to manipulate the qubit state, and finally are presented the dispersive limit and dispersive readout, as well as the two general mechanisms of decoherence.

2.1 Superconducting Qubits

2.1.1 Qubits

The classical bit can be in one of exactly two *states*, 0 or 1. It is the smallest unit of information. Classical computer memories are made up of many such bits, which together just constitute lists of zeros and ones. Similarly the quantum bit, or qubit, is the smallest unit of quantum information. It can take on the *states* $|0\rangle$ or $|1\rangle$. But due to its quantum mechanical nature, it can also be in a linear superposition state of both:

$$|\psi\rangle = \alpha\,|0\rangle + \beta\,|1\rangle\,. \tag{2.1}$$

The numbers α and β are complex numbers, and the states $|0\rangle$ and $|1\rangle$ are vectors living in a two-dimensional complex Hilbert space $\mathcal{H}$. When the qubit in the superposition state is measured, then the wavefunction $|\varphi\rangle$ collapses and the outcome is always either $|0\rangle$ or $|1\rangle$, but the probability of it being in $|0\rangle$ is $P_0 = |\alpha|^2$ and the probability of being in $|1\rangle$ is $P_1 = |\beta|^2$, with

$$|\alpha|^2 + |\beta|^2 = 1. \tag{2.2}$$

Up to here, a qubit is just a mathematical object describing any two-level quantum system. The $|0\rangle$ will represent the ground level in our experiments and $|1\rangle$ the excited level. In the physical world, this mathematical object exists and can be realized in many different ways. However, in all cases the system has to be quantum mechanical in order to allow the superposition of the states. Possible quantum systems used to implement qubits are quantum dots manipulating the spin of the electron [4], NMR techniques using the nuclear spin [5], [6], photons using the polarization [7], and cold ion traps engaging the electronic states of the ions [8]. One of the most promising systems for quantum computing are superconducting circuits using the energy states of a Cooper Pair Box coupled to a microwave resonator [9]. But before describing how these are implemented, we shall introduce the Bloch sphere representation of a qubit state. Indeed, this abstract representation is very useful because

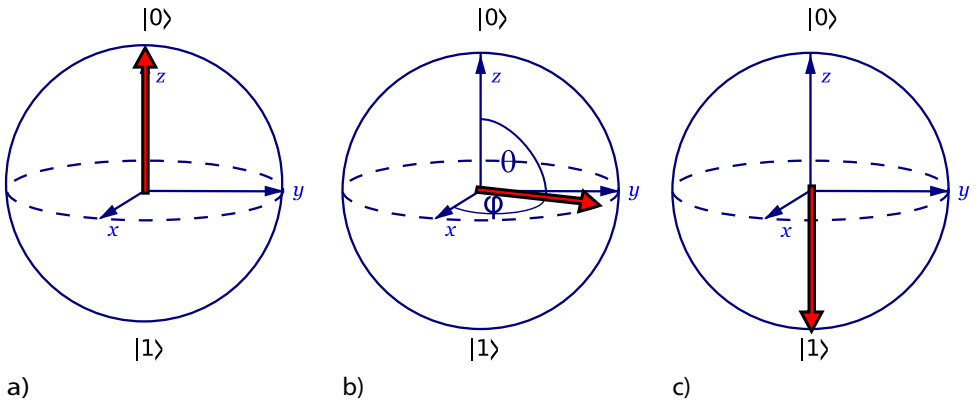

Figure 2.1: Bloch sphere representation of different qubit states: a) the ground state, b) an equal superposition state, c) the excited state. [10].

it allows us to geometrically visualize the dynamics and manipulation of any superposition state of the qubit.

Bloch sphere

Eq.(2.2) allows us to rewrite Eq.(2.1) in the following form

$$|\psi\rangle = \left(\cos\frac{\theta}{2}|0\rangle + e^{i\varphi}\sin\frac{\theta}{2}|1\rangle\right). \tag{2.3}$$

The polar angle θ and the azimuth angle φ create the unit three-dimensional Bloch sphere, shown in Fig. 2.1. The ground state $|0\rangle$ corresponds to a vector pointing to the north pole (a), the excited state $|1\rangle$ corresponds to a vector pointing to the south pole (c), and equal superposition states $1/\sqrt{2}\left(|0\rangle + e^{i\varphi}|1\rangle\right)$ are vectors pointing to the equator (b).

The Bloch sphere representation is unfortunately limited to one qubit, because a generalization to many qubits becomes too difficult to visualize.

2.1.2 Josephson junction

One of the criteria for building a quantum information processor is that the architecture must be scalable to large numbers of qubits. This is why superconducting charge qubits in circuit QED are so promising, because the qubits are nano-electronic devices based on Josephson junctions [11] which can be embedded in electronic circuits, and thus can be scaled up to many qubits. Furthermore, our system needs to have anharmonic energy levels for quantum computing and thus needs non-linear electrical elements in the circuit. Indeed, Josephson junctions are the only non-linear elements with no dissipation known for this purpose. This section describes the Josephson tunnel junction and the Cooper Pair Box, which form the building blocks of a superconducting charge qubit.

In the early twentieth century, quantum mechanics had revealed the quantum tunneling effect of single electrons flowing through an insulating barrier. It was not until 1962 that Brian David Josephson [12] discovered the tunneling of superconducting Cooper pairs across a weak link, for which he received the Nobel Prize in 1973. The weak link is achieved by separating two coupled superconductors with a thin insulating layer, creating thus a superconductor-insulator-superconductor junction, or Josephson junction (see Fig. 2.2).

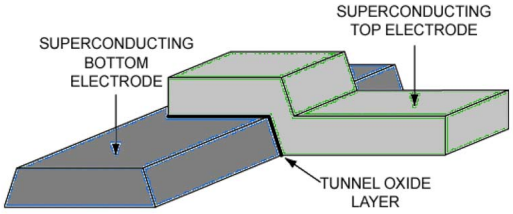

Figure 2.2: Josephson tunnel junction, the superconductors are made of Nb, Al, and the tunnel barrier is AlO_x. [13].

Each superconductor is described by a condensate wave function

$$\Psi_i = \sqrt{n_i^{CP}} e^{i\delta_i}, \tag{2.4}$$

where n_i^{CP} is the Cooper pair density and δ_i is the global phase, i indexing the two superconductors. Thus the phase difference across the Josephson junction is $\delta = \delta_1 - \delta_2$. There are two currents flowing through the junction. The first is the current arising from the tunneling of Cooper pairs, which we will describe now. The second is the current from quasiparticles, described in section 3.4. The Cooper pair tunneling current is described by two main effects:

1. **DC Josephson effect** - A DC current that flows across the junction due to tunneling is proportional to the sine of the phase difference across the tunnel barrier, giving the *Josephson or weak-link current-phase relation*

   $$I_t = I_c \sin\delta. \tag{2.5}$$

   The constant I_c is the *critical-current* giving the maximal DC current that can flow through the junction.

2. **AC Josephson effect** - When a voltage V is applied across the junction, the phase difference evolves linearly with time according to the *Superconducting phase evolution equation*

   $$\frac{\partial\delta}{\partial t} = \frac{2\pi V(t)}{\Phi_0}, \tag{2.6}$$

   where the physical constant $\Phi_0 \equiv \frac{h}{2e}$ is the magnetic flux quantum. Neglecting integration constants [14], this gives leads to

   $$\delta = \frac{2\pi V}{\Phi_0} t. \tag{2.7}$$

   Substituting this into Eq.(2.5) finally gives

   $$I(t) = I_c \sin\left(\frac{2\pi V}{\Phi_0} t\right). \tag{2.8}$$

   Thus the current will be an AC current with amplitude I_c and angular frequency $2\pi V/\Phi_0$.

The potential energy stored in the junction due to the voltage applied (inducing a supercurrent flowing through it) is given by

$$\begin{aligned} E &= \int IV\,\mathrm{d}t = \int I_c \sin\delta \frac{\Phi_0}{2\pi}\frac{\partial\delta}{\partial t}\,\mathrm{d}t = \frac{\Phi_0}{2\pi} I_c \int \sin\delta\,\mathrm{d}\delta \\ &= \frac{\Phi_0 I_c}{2\pi}\cos\delta \\ &= E_J \cos\delta. \end{aligned} \tag{2.9}$$

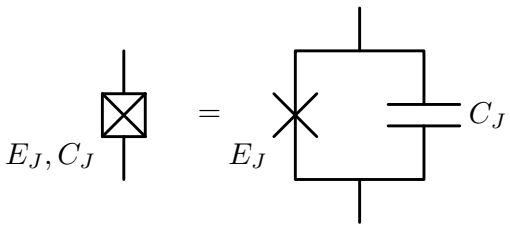

Figure 2.3: Circuit diagram of a Josephson junction.

The quantitiy $E_J \equiv \Phi_0 I_c/2\pi$ is called the *Josephson coupling energy.*

In addition, the total charging energy stored in the junction due to the n excessive Cooper pairs on one side is given by

$$U = \frac{1}{2}C_J V^2 = \frac{1}{2}C_J \left(\frac{n(2e)}{C_J}\right)^2 = \frac{(2e)^2}{2C_J}n^2 = E_C\, n^2, \tag{2.10}$$

where C_J is the total capacitance of the junction. The quantity $E_C \equiv (2e)^2/2C_J$, called *charging energy*, is the electrostatic energy needed to transfer one Cooper pair across the junction.

In a traditional circuit diagram, a real Josephson junction is represented by a crossed square (Fig. 2.3), and it is modeled by putting in parallel an ideal Josephson junction (a cross) characterized by its Josephson energy E_J and a capacitor C_J. The parameters E_J and C_J can be specified in the fabrication process by choosing the appropriate thickness and overlap area of the thin insulating layer of the junction.

Taking now the derivative of the first Josephson relation (2.5),

$$\dot{I} = I_c \cos\delta\, \dot{\delta}, \tag{2.11}$$

and inserting it into the second Josephson relation (2.6) gives

$$V = \frac{\Phi_0}{2\pi I_c}\frac{1}{\cos\delta}\dot{I} \equiv L_J\, \dot{I}. \tag{2.12}$$

The last equivalence is justified from comparing this expression with the expression for a voltage across a conventional inductance

$$V = L\dot{I}. \tag{2.13}$$

Thus the Josephson junction behaves like a non-linear inductor thanks to the Josephson inductance $L_J = L_0/\cos\delta$, which accumulates energy when a supercurrent passes through it. However, the accumulated energy is not in the form of magnetic field, but rather in the form of Josephson energy hidden inside the junction.

2.1.3 Cooper Pair Box

A Cooper Pair Box (CPB) is s simple quantum circuit used as a qubit. It is a small island connected on one side via a Josephson junction to a superconducting reservoir, and on the other side coupled to a control gate voltage V_g via a gate capacitor C_g, as seen in Fig. 2.4. The Hamiltonian of the Cooper Pair Box is

$$\mathcal{H}_{CPB} = E_C\,(N - N_g)^2 - E_J \cos\delta. \tag{2.14}$$

Here, the first term is the electrostatic energy of the CPB, where $E_C = (2e)^2/2C_\Sigma$ is the charging energy, i.e. the energy needed to add one additional Cooper pair onto the island,

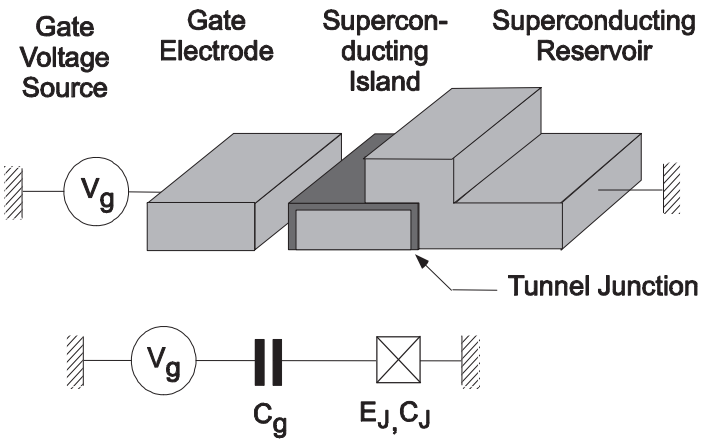

Figure 2.4: Schematic respresentation of a Cooper Pair Box and its corresponding circuit diagram. The Tunnel junction is the Josephson junction allowing Cooper pairs to tunnel onto the superconducting island. [15].

N is the number of excess Cooper pairs on the island, $N_g = C_g V_g/2e$ is the gate induced charge, and $C_\Sigma = C_g + C_J$ is the total capacitance. The second term is the energy stored in the Josephson junction which is responsible for the tunneling of Cooper pairs.

The only degree of freedom in the system is the number of excess or deficit Cooper pairs N on the island and it must be treated quantum mechanically as an operator $\hat{N}$. Through this quantization is then defined the conjugate operator $\hat{\delta}$ with the relation $\hat{\delta} = i\partial/\partial\hat{N}$ and $[\hat{\delta}, \hat{N}] = i$. With the help of the following two relations,

$$\cos\hat{\delta} = \frac{1}{2}\left(e^{i\hat{\delta}} + e^{-i\hat{\delta}}\right)$$

$$e^{\pm i\hat{\delta}}\,|N\rangle = |N \pm 1\rangle\,,$$

the Hamiltonian can be written in the eigenbasis of $\hat{N}$, giving

$$\hat{\mathcal{H}}_{CPB} = \sum_N [\, E_C(\hat{N} - N_g)^2\ |N\rangle\langle N| \ - \ \frac{E_J}{2}\,(\,|N\rangle\langle N+1| + |N+1\rangle\langle N|\,)\,]. \tag{2.15}$$

Fig. 2.5 shows the energy level diagram of this Hamiltonian. The dashed and dotted parabolas are simply the result of the electrostatic part of the Hamiltonian. Near the crossing of the parabolas, the two charge states become degenerate and the Josephson coupling mixes them and modifies the energy eigenstates. The ground and excited eigenstates are then superpositions $(|0\rangle \pm |1\rangle)/\sqrt{2}$, such that an avoided crossing appears. In vicinity of such degeneracy points the system effectively reduces to a two-state quantum system. Because the coupling energy E_J is only relevant for the ground and first excited states $|0\rangle$ and $|1\rangle$, higher energy levels are well separated from these first two levels, thus constituting an effective qubit.

Consider the Hamiltonian above (2.15) at $N_g = 1/2$. Taking the matrix form of the Hamiltonian for the two lowest energy states only, and performing a Taylor expansion, we obtain

$$\mathcal{H}_{N_g \approx \frac{1}{2}} = \begin{pmatrix} \frac{1}{2}E_C(2N_g - 1) & -\frac{E_J}{2} \\ -\frac{E_J}{2} & -\frac{1}{2}E_C(2N_g - 1) \end{pmatrix}.$$

The eigenvalues representing the ground and first excited state are

$$E_{0,1} = \pm\frac{1}{2}\sqrt{E_C^2(2N_g - 1)^2 + E_J^2}. \tag{2.16}$$

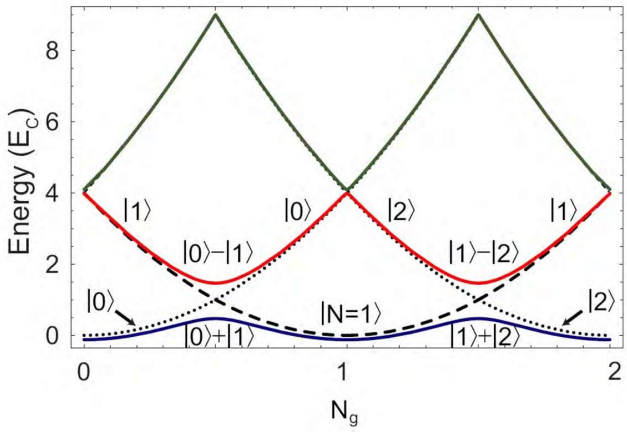

Figure 2.5: Energy level diagramm of the superconducting Cooper Pair Box, as a function of the gate charge $n_g \equiv N_g$. The different dashed parabolas represent a different number of excess Cooper pairs N on the island. The blue, red and green levels are the ground, first excited and second excited states. Here $E_C = E_J$. [16].

It is apparent now that at the degeneracy point, the energy difference between the two levels reduces to approximately E_J.

When biasing the gate voltage to one of the degeneracy points, for example $N_g = 1/2$, the CPB becomes insensitive to first-order fluctuations of the gate charge (noise)[17], because the slope of the charge dispersion at that point is null. For this reason we call this point the sweet spot.

2.1.4 Split Cooper Pair Box

The characteristic parameters E_C and E_J of the Cooper pair box are determined in the fabrication process. However, the number of excess Cooper pairs on the island N_g can be controlled via the gate voltage V_g. Yet one wishes to control the Josephson energy E_J as well, because it determines the frequency of the qubit at the sweet spot. This is achieved by splitting the Josephson junction into two equal junctions with characteristic Josephson energies ($E_{J,1}$, $E_{J,2}$) and phases ($\hat{\delta_1}, \hat{\delta_2}$). The Fig. 2.6 shows that the two junctions create a superconducting loop through which an external magnetic flux can be applied.

The Hamiltonian for the Josephson energy then has two equal contributions

$$\hat{\mathcal{H}}_{CPB,J} = E_{J,1} \cos \hat{\delta_1} + E_{J,2} \cos \hat{\delta_2}. \tag{2.17}$$

Flux quantization sets the relation between the phase difference of the two junctions and the magnetic flux flowing through the loop [16]

$$\delta_1 - \delta_2 = \frac{2\pi\Phi}{\Phi_0},$$

where $\Phi_0 = h/2e$ is the superconduction flux quantum. The two junctions being symmetric, this finally gives the single-junction Hamiltonian (2.14) with an effective Josephson energy

$$E_J = (E_{J,1} + E_{J,2}) \cos\left(\pi \frac{\Phi}{\Phi_0}\right), \tag{2.18}$$

which is tunable by an external magnetic flux Φ.

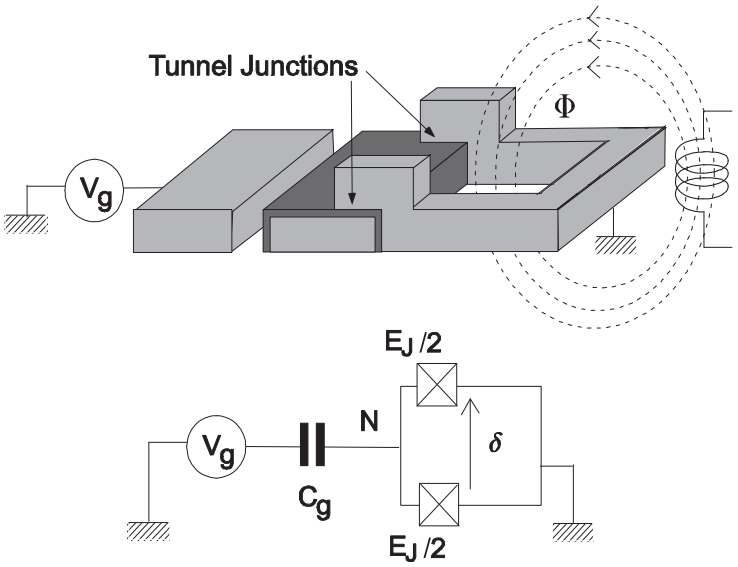

Figure 2.6: Schematic representation of a split Cooper pair box and its circuit diagram. The two symmetrical Josephson junctions allow for the magnetic flux through the created loop to tune the total Josephson energy, hence the transition frequency of the qubit.

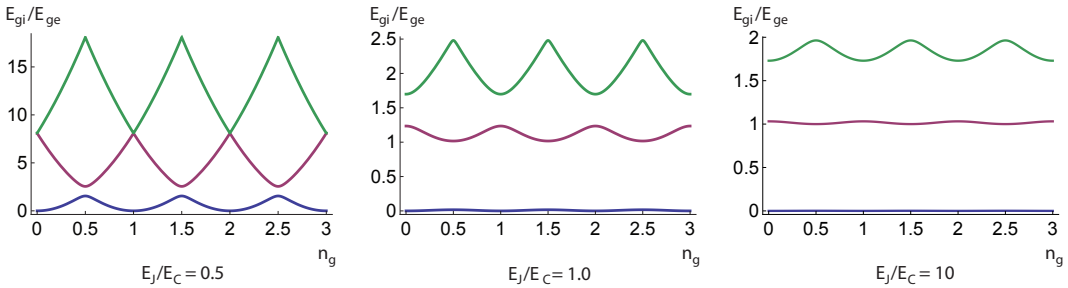

Figure 2.7: Energy diagram of the first three eigenenergies of the qubit Hamiltonian, expressed in units of the transition energy E_{eg}, as a function of the gate charge n_g, for different ratios of E_J/E_C. The higher ratios lead to a transmon. [19].

2.1.5 Transmon

For the sake of quantum computing, qubits need long coherence times. The question arises, what values for E_C and E_J allow the longest coherence times? In the case of the CPB, the charging energy is much larger than the Josephson energy, $E_C \gg E_J$ (charge regime). As the energy diagram shows a large charge dispersion, the device is then highly sensitive to charge noise, which changes the qubit transition frequency and thereby causes dephasing. As explained above, operating at the sweet spot reduces this effect substantially, but the coherence time of the split CPB is still limited by higher-order effects [18]. Also, in reality it is difficult to keep the system at the sweet spot without having to constantly reset the gate voltage. Fortunately, operating in a different regime where the Josephson energy is much larger than the charging energy, $E_J \gg E_C$, the energy levels exponentially flatten out (decrease of the charge dispersion, cf. Fig. 2.7) and become insensitive to the change in gate charge N_g. A split Cooper pair box operated in the regime $E_J/E_C \approx 10$ is called a transmon.

It is important to note that as the ratio is increased, the anharmonicity decreases. Choosing a too big ratio would not allow a selective control of the transitions anymore. A correct

balance must therefore be found between charge noise insensitivity and anharmonicity. Physically, the ratio E_J/E_C is increased by increasing the total capacitance $C_\Sigma \propto 1/E_C$ of the transmon. This is achieved by adding a shunt capacitor C_B and fabricating the capacitor of the junction in the shape of a zipper in order to increase the total area (cf. Fig. 2.9 and Fig. 3.1).

The transmon qubit will be integrated in a circuit, where it is coupled to a microwave resonator. Microwave pulses will excite the qubit, if their frequency matches the transition frequency of the qubit. This is approximately given by [17]

$$\hbar\omega_{01} \approx \sqrt{8E_C E_J^{max} |\cos(\pi \frac{\Phi}{\Phi_0})|} - E_C, \tag{2.19}$$

with the anharmonicity given by

$$\hbar\omega_{12} - \hbar\omega_{01} \approx -E_C. \tag{2.20}$$

2.2 Circuit QED

2.2.1 Cavity Quantum Electrodynamics

For quantum computing, one wishes to manipulate and readout the states of qubits. What physical interactions can be used to achieve this? Since the transmon is a two-level system that behaves like a single atom, one can use cavity quantum electrodynamics. It studies the interaction between photons and atoms in a cavity. Optical or microwave photons are sent through a highly reflective cavity where they get confined (bounce back and forth) and form quantized electromagnetic modes. The advantage is that high coupling strength for the electric dipole interaction is achieved even with just a single photon in the cavity. The photon modes can be described as excitations of a quantized harmonic oscillator, which then interact with the two-level system (the qubit), illustrated in Fig. 2.8. The interactions of this system are described by the Jaynes-Cummings Hamiltonian [9]

$$H = \hbar\omega_r \left(a^\dagger a + \frac{1}{2}\right) + \frac{1}{2}\hbar\omega_a \sigma_z + g\hbar(a^\dagger \sigma^- + a\sigma^+) + H_\kappa + H_\gamma. \tag{2.21}$$

The first three terms describe the coherent dynamics of the photon-atom system, whereas the two last terms describe decoherence effects of the system. The first term is the usual energy of a quantum harmonic oscillator, describing here the energy from the photons in the cavity. The operators $a^\dagger$ and a are the photon creation and annihilation operators, and each photon has the energy $\hbar\omega_r$. The second term describes the energy of the atom as a two-level system with transition energy $\hbar\omega_a$, with spin eigenstates measured along the z-axis by the Pauli z-operator $\sigma_z = (|1\rangle\langle 1| - |0\rangle\langle 0|)$. The third term describes the interaction between the photons and the atom. It contains the coupling strength g which expresses the rate at which the atom absorbs photons via $a\sigma^+$ and emits photons via $a^\dagger\sigma^-$, where $\sigma^+ = |1\rangle\langle 0|$ and $\sigma^- = |0\rangle\langle 1|$. Furthermore, the term H_κ expresses the dissipative loss from the fact that the cavity is coupled to the environment. There is a photon decay rate κ which is determined by the ratio of the resonance frequency and the quality factor of the cavity $\kappa = \omega_r/Q$. The last term expresses the coupling of the atom to modes other than the cavity mode which cause the excited state to decay at rate γ

Reducing the decay times by engineering a high-Q cavity and creating large fields in the cavity allows for strong interaction, called strong coupling regime $g \gg \kappa, \gamma$. This regime allows for vacuum Rabi oscillations, where the atom constantly absorbs and reemits a photon at the Rabi frequency g/π [20].

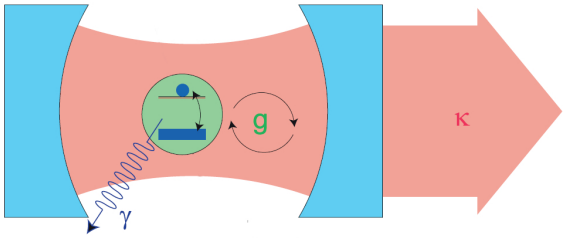

Figure 2.8: A schematic representation of cavity QED. The atom placed in the high quality cavity constantly absorbs and re-emits the trapped photons. Strong coupling is achieved when the coupling strength is much larger than the decay rates of the cavity and atom. [16].

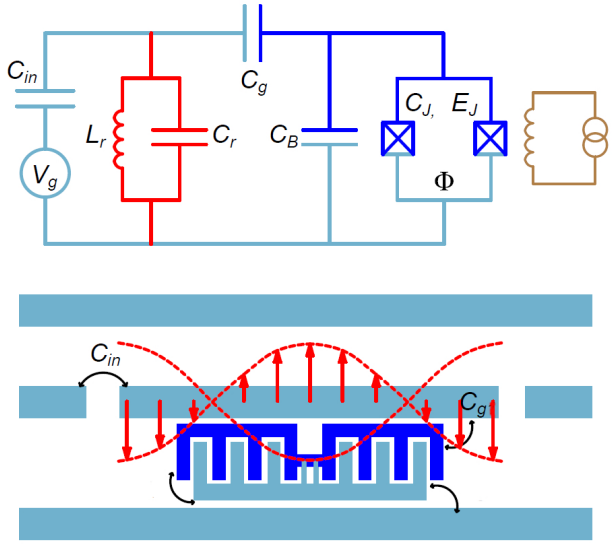

Figure 2.9: Circuit QED. Top: circuit diagram of the split Cooper Pair Box coupled to the resonator. Bottom: schematic representation of the transmon coupled to the coplanar waveguide resonator. [16].

2.2.2 Coplanar waveguide resonator

In circuit QED, the transmon qubit plays the role of the atom from cavity QED, and an electrical resonator plays the role of the cavity. The electric field of the standing waves trapped in the resonator couple to the qubit. In our case the resonator is 1D transmission line resonator, which is capacitively coupled to input and output lines, and which can be modeled by an LCR oscillator. The transmission line though is modeled with the distributed element model, because microwaves are high-frequency waves and have wavelengths which approach the physical dimensions of the circuit, making thus the lumped model inaccurate. The theory of transmission lines is well presented in [14]. In our experiments, the 1D transmission line resonator is physically realized with a coplanar waveguide resonator (CWR), depicted in Fig. 2.9. It resembles the cross section of a coaxial cable in two-dimensions. The fact that the resonator is one dimensional constrains the electromagnetic field into a smaller volume than a 3D cavity, thus rendering a higher intensity and stronger coupling.

The superconducting qubit is embedded in the circuit at a spot where the intensity of the electric field of the standing wave in the resonator has a maximum. The gap between the center conductor of the coplanar waveguide and the island of the transmon acts as the gate capacitor (C_g in Fig. 2.9) to control the tunneling of the Cooper pairs between the island

and the reservoir. For this a DC gate voltage V_{DC} is applied on the center conductor over the input gap capacitor C_{in}. Additionally, the photons in the cavity build up a quantum voltage $\hat{V}$ in the resonator. The gate voltage applied to the split Cooper pair box is then

$$V_g = V_{DC} + \hat{V}.$$

Since the resonator can be modeled as an electrical LC circuit, the charge operator $\hat{q}$ is found from the traditional quantization of a classical harmonic LC oscillator and is expressed in terms of the creation and annihilation operators

$$\hat{q} = i\sqrt{\frac{\hbar}{2Z_c}}(a^\dagger - a),$$

with $Z_c = \sqrt{L/C} = \omega_r C$ is the characteristic impedance of the circuit. Substituting this into $\hat{V} = \hat{q}/C$ leads to the quantum gate voltage

$$\hat{V} = \sqrt{\frac{\hbar\omega_r}{2C}}(a + a^\dagger) = V_0(a + a^\dagger),$$

where V_0 is the rms vacuum fluctuations. Plugging this into the $\mathcal{H}_{el}$ in (2.14) and expanding the square, one obtains a new term describing the cavity-qubit coupling

$$\begin{aligned} \mathcal{H}_{int} &= 2\hbar g(a + a^\dagger)\hat{N}, \\ g &= \frac{C_g}{C_\Sigma}\frac{eV_0}{\hbar}. \end{aligned} \tag{2.22}$$

Ignoring fast oscillating terms $a^\dagger\sigma^+$ and $a\sigma^+$ via the rotating wave approximation, the Hamiltonian reduces to

$$\mathcal{H}_{int} = \hbar g\left(a^\dagger |0\rangle\langle 1| + a|1\rangle\langle 0|\right). \tag{2.23}$$

Combining this interaction Hamiltonian with the single mode cavity Hamiltonian and the two state qubit Hamiltonian, we retrieve the Jaynes-Cumming Hamiltonian (2.21).

2.2.3 External drive

The Jaynes-Cummings Hamiltonian (2.21) describes in one of its terms the energy of the qubit as $\hbar\omega_{01}\sigma_z/2$ with its transition frequency ω_{01}. For the sake of quantum computing, one needs a channel to read out the state of the qubit and at the same time a channel to control it. Thus it is of advantage to use an external gate line to drive the qubit, and use the resonator as readout channel. Just as a single isolated spin (a two level system) reacts to an applied external magnetic field, the state of the superconducting qubit reacts to an external EM field with frequency ω, phase ϕ, and amplitude ϵ. This external drive is implemented by sending a microwave signal through an additional transmission line capacitively coupled to the transmon (cf. single charge line entering the chip from the left side in Fig. 3.1). The Hamiltonian for the energy of the qubit then gains an additional term giving

$$\mathcal{H} = \frac{1}{2}\hbar\omega_a\sigma_z + \hbar\epsilon\cos(\omega t + \phi)\sigma_x. \tag{2.24}$$

The drive term is time dependant and has a high frequency ω in the order of gigahertz. This means that the electronics would need to have a time resolution of less than 100 picoseconds to drive the qubit in a time which is smaller than the time of one frequency oscillation. Changing to the rotating frame makes life easier. For the Heisenberg picture the time evolution operator

$$U(t) = e^{i\frac{\omega t}{2}\sigma_z}, \qquad \text{with } [U, \sigma_z] = 0 \quad \text{and} \quad [U, \sigma_x] \neq 0,$$

transforms the old Hamiltonian into

$$\begin{aligned}\tilde{\mathcal{H}} &= U(t)\ \mathcal{H}\ U^\dagger(t) - i\hbar\, U(t)\frac{\partial U^\dagger(t)}{\partial t} \\ &= \frac{1}{2}\hbar\omega_a\ \sigma_z\ e^{i\frac{\omega t}{2}\sigma_z}\ e^{-i\frac{\omega t}{2}\sigma_z} \\ &\quad + \hbar\epsilon\cos(\omega t+\phi)\ e^{i\frac{\omega t}{2}\sigma_z}\ \sigma_x\ e^{-i\frac{\omega t}{2}\sigma_z} \\ &\quad - i\hbar\ e^{i\frac{\omega t}{2}\sigma_z}\left(-i\frac{\omega}{2}\sigma_z\right)e^{-i\frac{\omega t}{2}\sigma_z} \\ &= \frac{\hbar\omega_a}{2}\sigma_z + \hbar\epsilon\cos(\omega t+\phi)\left[\cos(\omega t)\sigma_x - \sin(\omega t)\sigma_y\right] - \frac{\hbar\omega}{2}\sigma_z.\end{aligned}$$

Using the identity $\cos(\alpha) = (e^{i\alpha} + e^{-i\alpha})/2$,

$$\begin{aligned}\tilde{\mathcal{H}} = \frac{\hbar(\omega_a-\omega)}{2}\sigma_z + \frac{\hbar\epsilon}{4}[&(e^{i(2\omega t+\phi)} + e^{-i(2\omega t+\phi)} + e^{-i\phi} + e^{i\phi})\sigma_x \\ &+ i(e^{i(2\omega t+\phi)} + e^{-i(2\omega t+\phi)} + e^{i\phi} - e^{-i\phi})\sigma_y].\end{aligned}$$

This Hamiltonian contains exponential terms with arguments in ω. These are fast oscillating terms, since the frequency ω is high. In the rotating wave approximation (RWA) we neglect these terms and keep only the slow oscillating terms in the rotating frame. Although, for it to be valid, the detuning $\omega_a - \omega$ and the amplitude ϵ must be small. The Hamiltonian then reduces to

$$\tilde{\mathcal{H}} = \frac{\hbar}{2}(\omega_a-\omega)\sigma_z + \frac{\hbar\epsilon}{2}(\cos\phi\sigma_x + \sin\phi\sigma_y). \tag{2.25}$$

Note that the time-dependance has been removed through the rotating frame and RWA. This two-level Hamiltonian is analogous to the one of a spin-$\frac{1}{2}$ in a static magnetic field

$$\mathcal{H} = -\frac{1}{2}\hbar\,\vec{B}\cdot\vec{\sigma}, \tag{2.26}$$

with $\vec{B} = (B_x, B_y, B_z) = (\epsilon\cos\phi\,,\ \epsilon\sin\phi\,,\ \omega_a - \omega)$.
This analogy allows us to represent the evolution of the two-level state on the Bloch sphere Fig. 2.1. As stated in the beginning of this section, for quantum computing we want to use the external drive (2.24) to manipulate the state of the qubit. In principle the qubit is found in the ground state as long as no drive is applied. Consider wanting to excite the qubit from the ground state $|0\rangle$ into the superposition state $1/\sqrt{2}(|0\rangle + |1\rangle)$, which corresponds on the Bloch sphere to performing a rotation of $\phi = \pi/2 = 90°$ around the $y-$axis, with a zero detuning $\omega_a - \omega = 0$. The driving field should thus be set as $\vec{B} = (0, \epsilon, 0)$. The driving Hamiltonian becomes $\mathcal{H} = \frac{1}{2}\hbar\epsilon\sigma_y$ which states that the Bloch vector starts to precess with frequency ϵ around the $y-$axis. The condition $\epsilon t = \pi/2 \Rightarrow t = \pi/2\epsilon$ determines how long the drive must be applied in order for the state vector to stop precessing exactly at the right point.

2.2.4 Dispersive limit and dispersive readout

The resonator can be used as an indirect measurement channel for Quantum Non-Demolition (QND) measurements, in addition to mediating the interaction between qubits. One drives the resonator at its resonance frequency and measures the transmission by operating the Jaynes-Cummings Hamiltonian in the dispersive limit [9], where the transition frequency of the qubit ω_a is far detuned from the resonance frequency of the cavity ω_r. This happens when $\Delta = \omega_a - \omega_r \gg g$, because the coupling is then too small to induce any transitions of the qubit, but there is still a dispersive interaction which we can make use of to determine the state of the qubit. Treating the Hamiltonian perturbatively by expanding in powers of g/Δ up to second order gives [17]

$$\mathcal{H}_{eff} = \frac{1}{2}\hbar\omega_a\hat{\sigma_z} + \hbar(\omega_r + \frac{g^2}{\Delta}\hat{\sigma}_z)(\hat{a}^\dagger\hat{a} + \frac{1}{2}) \tag{2.27}$$

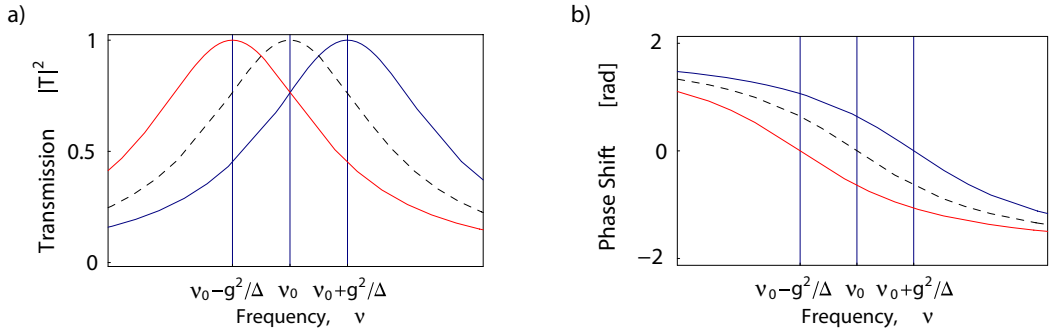

Figure 2.10: a) Amplitude of the transmission through the resonator. The dotted line represents the bare resonator frequency with no presence of a qubit. The other two lines represent the transmission at a shifted resonance frequency, depending on the state of the qubit, red if the qubit is in the ground state, blue if excited state. b) Phase of the transmitted microwaves depending on the qubit state. [21].

The first term is that of a harmonic oscillator with a shifted frequency. This result shows that the presence of the qubit shifts the resonance frequency ω_r of the cavity by g^2/Δ. Note that this shift is dependant on the state σ_z of the qubit, so the two level system of the qubit is mapped onto the positive or negative shift of the bare resonator frequency. This fact is used to perform a QND measurement of the qubit state. We send a microwave drive through the resonator and measure the transmission and phase of the transmitted microwaves, because the phase is given by $\delta\Phi = \pm\tan^{-1}(2g^2/\kappa\Delta)$ and reflects the shift as well. Fig. 2.10 a shows the transmission amplitude as a function of the frequency of the microwave drive. It is apparent that the peaks in transmission appear at different resonance frequencies of the cavity, depending on the qubit state. Fig. 2.10 b) shows the phase shift as a function of the frequency of the drive. If the qubit is in the ground state, the transmitted signal gets a zero phase shift when it is sent at $\nu_0 - g^2/\Delta$. Whereas if the qubit is in the excited state, the transmitted signal gets a zero phase shift at $\nu_0 + g^2/\Delta$. This allows us to infer the state of the qubit.

2.3 Decoherence

The greatest challenge with the physical realization of quantum bits is suppressing decoherence mechanisms. The qubit is naturally coupled to the environment and therefore undergoes entanglement with it. The quantum entanglement causes the qubit to loose its defined quantum state over time, resulting in decoherence which can be categorized into two forms: energy relaxation and dephasing [22].

Energy relaxation is the process of decay from the excited state to the ground state due to the interaction with noise form the environment which has frequencies close to that of the qubit transition frequency. This mechanism is represented in the Bloch sphere in Fig. 2.11(left). The time which the excited state takes to decay into the ground state $T_1 = 1/\Gamma_1$ is the inverse of the relaxation rate Γ_1. If one could perfectly isolate our quantum system from the environment, there would be no energy relaxation. Also, we cannot completely decouple our system from the environment, because we still need to be able to manipule the state of the qubit for quantum computing.

The dephasing is the loss of knowledge about the phase of the quantum state, as repre-

sented in Fig. 2.11(right), with

$$\frac{1}{T_2} = \frac{1}{2T_1} + \frac{1}{T_\phi} \tag{2.28}$$

The first contribution arises from the energy decay and the second, called pure dephasing, arises due to random variation of the qubit frequency induced by low frequency 1/f noise.

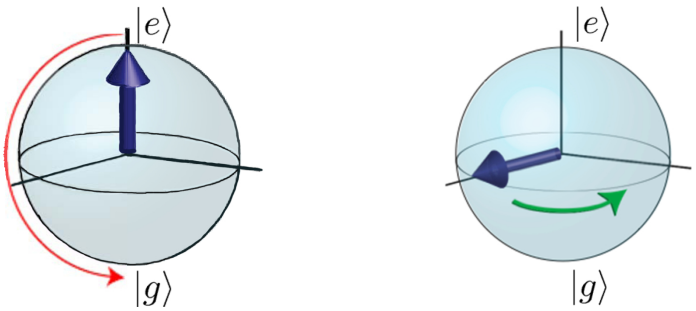

Figure 2.11: a) Bloch sphere representation of the energy relaxation of the the excited state Bloch vector. b) representation of the dephasing mechanism on the qubit state which acquires a random phase.

Chapter 3

Measurement Setup

Circuit QED is performed with an on chip resonator and embedded qubits in the microwave regime. In order for the qubits to show long coherence times for quantum computing, the experimental setup has to satisfy many difficult criteria concerning signal generation, data acquisition, signal filtering and attenuation, and thermal isolation. In this section we discuss how these issues are experimentally handled.

3.1 The sample

In our experiment, the quantum device used is a 8-port sample shown in Fig. 3.1 consisting of a coplanar waveguide resonator with three transmons. The qubits are embedded at the spots of maximum electric field of the standing waves in the resonator, achieving strong coupling there. The typical size of the elements is characteristic of the microwave wavelengths, corresponding to frequencies in the order of several hundred MHz to a few GHz. The resonator is made of Niobium on a sapphire substrate fabricated by optical lithography. A detailed description about the fabrication of the sample can be found in [23]. The superconducting islands of the transmons are fabricated by electron beam lithography and made of aluminium, and the tunnel barriers of the Josephson junctions are aluminium oxide. The sample is fixed on a printed circuit board (PCB) shown in Fig. 3.2(right), where each of the 8 visible cable connectors leads with a transmission line to the input ports of the sample.

The important parameters E_C and E_J and g were engineered [24], [25] such that the three qubits all have well separated maximum transition frequencies and that the requirement of anharmonicity is fulfilled.

The bare resonator frequency of the resonator is $\nu_r = 8.625$ [GHz] and its quality factor is $Q = 3300$.

As presented in subsection 2.1.4 and 2.1.5, the qubit Josephson energy and thus directly the qubit frequency may be tuned via (2.19) by applying an external magnetic flux through the superconducting loop formed by the two Josephson junctions in the split Cooper Pair box. Since our sample has three transmon qubits, we need three magnetic coils to tune each qubit separately. The coils should be placed as close as possible to the sample. Therefore, the PCB is placed directly on a copper housing enclosing the three coils, as indicated in Fig. 3.3. The big coil and the two small coils are screwed on the middle lid. The bottom lid serves as a protection of the coils from the embedding in epoxy (see chap. 4). Additionally,

	ν^{max} [GHz]	$E_C/\hbar$ [GHz]	$g/2\pi$ [MHz]
Qubit A	6.714	0.264	360
Qubit B	6.050	0.296	300
Qubit C	4.999	0.307	340

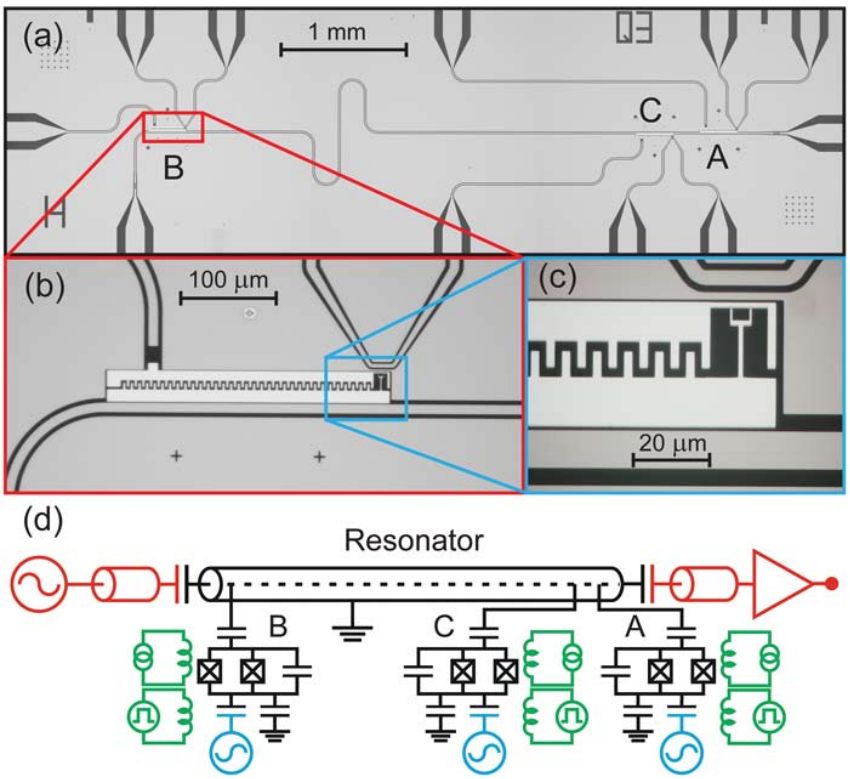

Figure 3.1: (a) An optical microscope picture of the 8-port sample. One recognizes the resonator crossing the chip horizontally and the three qubits A,B,C. (b) a zoom up on qubit B, the finger capacitor of the transmon becomes apparent. (c) a zoom up on the split Josephson junction of qubit B. (d) Circuit diagram of the sample.

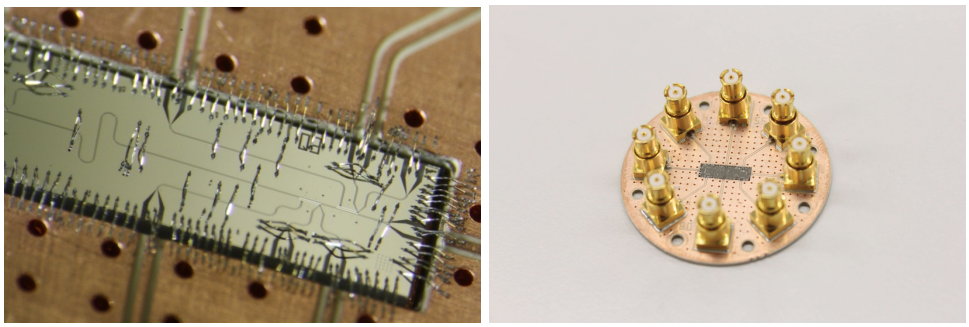

Figure 3.2: (Left) A picture of the sample glued onto the PCB and connected to it through the many wire bonds seen. (Right) A picture of the entire PCB. The microwave cables are connected to the 8 SMP connectors on the PCB, and the microwaves are then led by transmission lines on the PCB to the input ports of the sample.

a PCB cover is placed over the PCB to suppress the cylindrical electric field modes in the cavity formed between the PCB and the top lid. Fig. 3.3 shows all components of the so-called sampleholder.

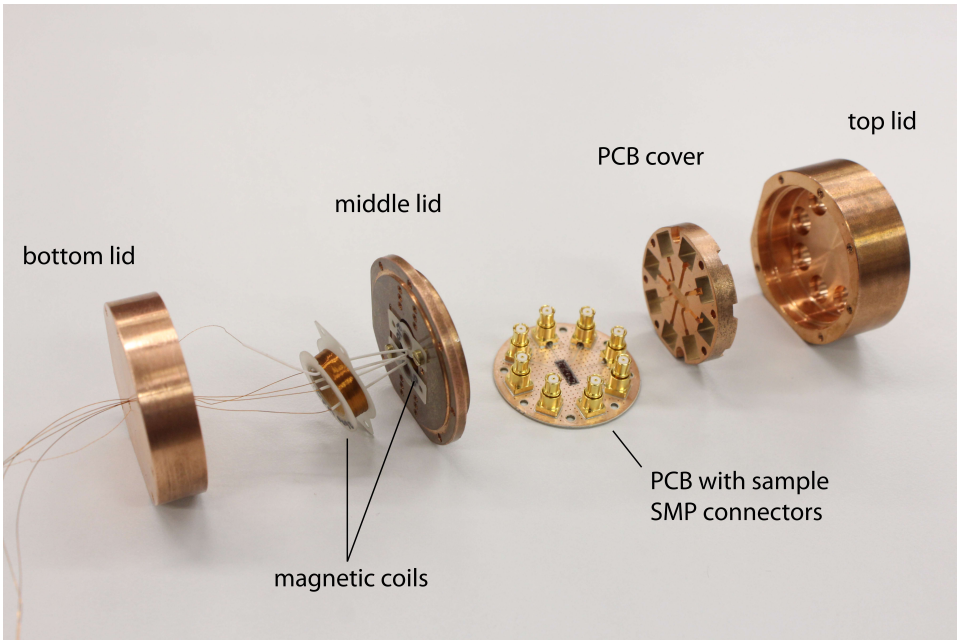

Figure 3.3: A picture of all the components of the sampleholder. The bottom, middle, and top lid form the box. The PCB is fixed onto the middle lid and covered by the PCB cover. Three magnetic coils are placed underneath the middle lid and have their wires leave the box throught a small central hole in the bottom lid.

A criteria for quantum computing is that one can initialize all states to the ground state. To make sure all qubits stay in the ground state as long as we don't intentionally excite them, the possibility of thermal excitation must be suppressed. The transition energy of the qubits must be much larger than the thermal energy $k_B T$. To satisfy this condition, one is tempted therefore to simply operate in much higher frequencies. However, higher frequency electronics leads to more noise, and also modern electronics equipment is limited and cannot process at too high frequencies. One must therefore operate at very low temperatures, $T \approx$ 20 mK, to suppress thermal excitation. Furthermore, the circuit must be superconducting for the Josephson effect to appear and losses to be low. For these reasons, the sample is placed inside a dilution refrigerator (DR).

3.2 The Dilution Refrigerator

The cryostat used is a Kelvinox 400HA dilution refrigerator from Oxford Instruments achieving a base temperature of $\sim$ 20 mK. Since the transmons have an energy scale of $\sim$1-10 GHz, the temperature in the cryostat must be at most 50-500 mK, which can only be reached with a DR. Details on the functioning of a DR can be found in [26]. Niobium and Aluminium are superconducting at these temperatures. Operating the superconducting circuit placed at the bottom of the DR requires wiring through the different temperature stages of the DR onto the microwave electronics equipment placed outside the DR at room temperature. The microwave signals sent from the signal generators down to the sample carry with them electrical noise and a heat load that must be suppressed, because the noise destroys the coherence of the qubits and the heat disturbs the smooth operation of the DR. This is achieved

by placing a number of attenuators on the microwave lines at different stages of the in-way, as represented in Fig. 3.4. The in-lines are thermally anchored at each temperature stage of the DR to reduce the heat transfer down to the sample. The transmitted signal through the resonator has very low power, on the order of 10^{-17} W, populating the resonator with only a few photons on average. The outcoming signal must then be amplified again on the way out for it to be detectable and read-out by the acquisition card. The electrical noise added in the amplification process is minimized by using low-noise amplifiers. Furthermore, to avoid noise and heat going back through the outline into the sample, the lines pass through two circulators which only allow signals to pass in the out direction.

3.3 Measurement instruments

The continuous and pulsed coherent microwaves used for the qubit readout and qubit manipulation are generated using an arbitrary waveform generator (AWG) and microwave generators. In order to produce very precise shapes of the pulses for the preparation of the qubit states, the amplitude, phase and frequency of the signals must be accurately controlled. This is only possible by upconverting the envelope pulses from the AWG by mixing them with a microwave tone. The mixer has two input ports, I and Q, one RF input, and one RF output. The RF input is split into two parts, one which is multiplied with the I quadrature input and the other, phase shifted by 90° multiplied with the Q quadrature input. The mixer then combines these two again to form the output RF signal composed of two different frequencies called sidebands. This method allow us to control amplitude and phase of the output RF signal that is sent to the chip simply by controlling voltages applied

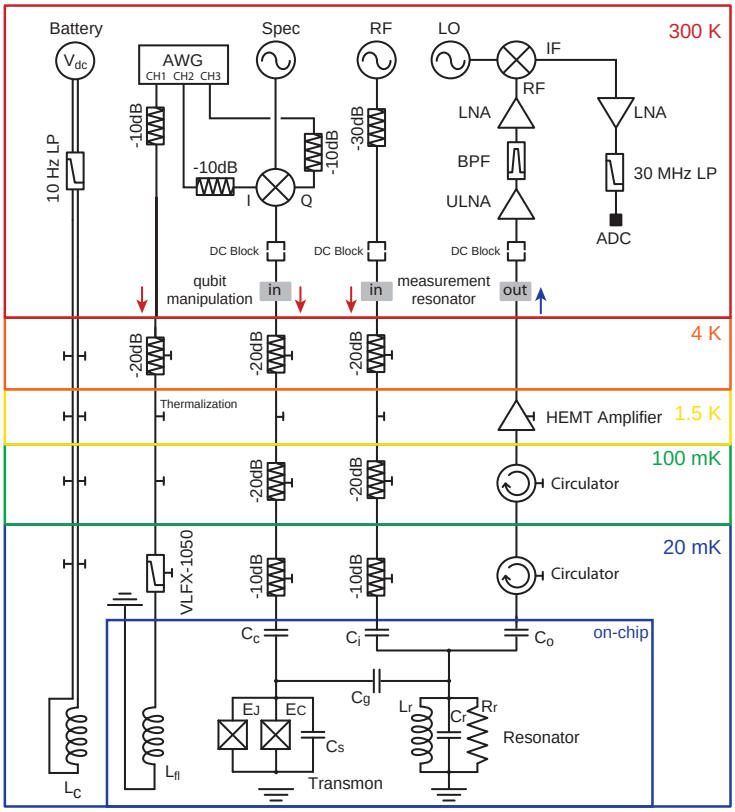

Figure 3.4: A schematic representation of the cryogenic measurement setup. Details can be found in [27].

to the I and Q ports.

The microwave signals produced and transmitted through the resonator of the superconducting circuit have a frequency of a few GHz, but the data acquisition card that reads out the signal in the end has a limited sampling rate (1 GS/s), and therefore the signal needs to be down-converted in frequency. This is done with an IQ mixer, which has two input ports an two output ports. One input is the transmitted signal (RF) which is split into two parts of equal amplitude. The other input is the local oscillator (LO) which is a signal of a frequency typically about $\omega_{LO} = \omega_{RF} - 25$ MHz lower than the RF, and which also gets split into two equal parts, but shifted by 90°. Mixing the four signals creates the two output lines. These are called I and Q quadratures and each of them is a superposition of two waves, one at $\omega_{RF} - \omega_{LO}$ and one at $\omega_{RF} + \omega_{LO}$. Passing the quadratures through a low pass filter eliminates the fast oscillating components and leaves only the component at a now much lower frequency of about 25 MHz. The two output quadratures I and Q can now be acquired by the card. The amplitude of the original signal is recovered by $\sqrt{I^2 + Q^2}$ and the phase is $arg(I + iQ)$. A more detailed description can be found in [28].

3.4 Sources of decoherence from the DR

As presented in the theory chapter, the Cooper Pair Box has only one discrete degree of freedom: the number of Cooper pairs on the island, which is controlled with the gate voltage and magnetic flux. Long coherence times are required for processing applications with the qubits and there are many different known sources of decoherence. One such problematic source is the tunneling of quasiparticles, even just a single one, on the island leading to relaxation and dephasing of the qubit [17]. The quasiparticles appear either due to an overall odd number of electrons (leaving one unpaired electron) or thermal breaking of Cooper pairs in the superconductors. From [17], we estimate the resulting contribution from quasiparticles to the relaxation of the qubit. For temperatures T small compared to the superconducting gap Δ, the number of quasiparticles in the system can be obtained as

$$N_{qp} = 1 + \frac{3\sqrt{2\pi}}{2} N_e \frac{\sqrt{\Delta k_B T}}{E_F} e^{-\Delta/k_B T}, \tag{3.1}$$

with N_e being the total number of conduction electrons in the qubit metal volume V. The first term, the constant 1, accounts for the possible one unpaired electron naturally present if V contains an odd number of electrons. The second term expresses the "equilibrium" finite probability of thermal breaking of the Cooper pairs. Calculating the rate of tunneling Γ_{qp} for one quasiparticle across the junction and the Franck-Condon factor matrix element, and disregarding possible non-equilibrium quasiparticle distributions, the full relaxation rate caused by quasiparticle tunneling is given by

$$\Gamma_1 = \frac{1}{T_1} \simeq \Gamma_{qp} N_{qp} \sqrt{\frac{k_B T}{\hbar \omega_{01}}} |\langle g, n_g \pm \frac{1}{2}| \, |e, n_g\rangle|^2. \tag{3.2}$$

Fig. 3.5 depicts T_1 and N_{qp} as a function of temperature, with typical transmon parameters inserted into the Eq.(3.2).

It shows that below approx. 100 mK our relaxation time should not be limited by the equilibrium quasiparticles, since the exponential term in Eq. (3.2) becomes negligibly small. A significant drop off only occurs for higher temperatures. In our case, our sample is for instance placed in the cryostat at a base temperature T≈ 25 mK. This theory tells us then that in principle, we should not worry about equilibrium quasiparticles limiting our T_1 times, and that the relaxation is due to some other sources. However, the superconducting qubits research group at IBM T.J. Watson Research Center [29] recently performed experiments which suggest that non-equilibrium quasiparticles take effect. They obtained that the relaxation time might well be limited by some "external loss process due to quasiparticles

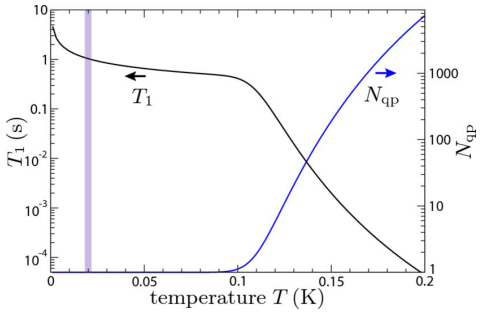

Figure 3.5: Number of quasiparticles and contribution to the relaxation time T_1 due to equilibrium quasiparticle tunneling as a function of temperature. At cryogenic temperatures, the transmon should not be limited by this effect. Graph taken from [17].

generated by radiation of energy (>80 GHz) which exceeds the superconducting gap of Al ($\Delta \approx 200\ \mu$eV)". Indeed, the experiment that the IBM group performed with a flux qubit consisted of embedding the sample into a microwave absorptive medium, resulting in a T_1 improvement of 10 times, from ≈ 500 ns to $\approx 5\ \mu$s. The improvement is attributed to the suppression of external radiation that generated the "non-equilibrium" quasiparticles. The energy 200 μeV of the gap corresponds to an energy scale of 48 GHz. Within the Dilution Refrigerator, blackbody radiation is constantly emitted from the different temperature stages. From Wien's displacement law, blackbody radiation from the temperature stage of 1.5 K (1K pot) has a peak emission at a frequency ν_{max} =1.5 K $\times$ 58.8 GHz K^{-1} $\approx$ 88 GHz, and the 800 mK stage has ν_{max} = 47 GHz, and the 1.7 K stage has ν_{max} = 100 GHz. This last radiation has an energy exceeding two times the superconducting gap, which is the energy needed to break a Cooper pair. The radiation from these stages can presumably find ways to propagate down to the base of the DR and generate the so-called non-equilibrium quasiparticles which have detrimental effects on the coherence time of the qubit.

Furthermore, to "mimic the effect of quasiparticles generated by radiation" in the experiment before the embedding, they measured the T_1 for higher base temperatures, the result is shown in their Fig. 3.6.

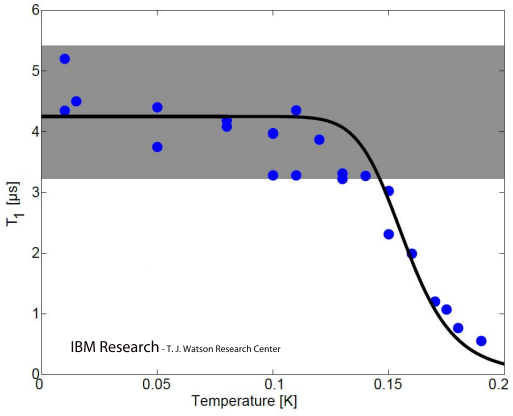

Figure 3.6: Picture taken from [29]. "T_1 versus mixing chamber temperature. Shaded area indicates range of T_1 consistent with repeated measurements. The drop off of T_1 above 150 mK is in agreement with quasiparticle generation (theory solid line)".

A roll-off of T_1 occurs around 140 mK, and it drops to 0 around 200 mK. This result is in agreement with the above theory of equilibrium quasiparticles in Eq.(3.2). This is the hint that the quasiparticles are indeed the limiting source of decoherence. For this reason, we tried the same procedure of embedding our sample in a microwave absorptive medium, and test if the suppression of quasiparticles also leads to an improvement of T_1 and T_2 in the transmon.

Chapter 4

Design and construction of the Eccosorb box

This chapter will explain how the microwave absorptive box around the sampleholder was built. The absorptive medium used is a two part castable magnetically loaded absorber epoxy from the company Emerson & Cumming, called the ECCOSORB CR-124, shown in (Fig. 4.1(bottom left).

We embedded the sampleholder in this Eccosorb, forming an absorptive box around it, with the goal of protecting the sample from external radiation from the DR. The final box is shown in Fig. 4.1(top), with a close-up view in the bottom right photo. As opposed to the embedding from the IBM group, our box is built in two parts such that one can open and close it to exchange the PCB and the sample.

Fig. 4.2 shows all the assembled components of the box. One recognises the different parts: the top and bottom part of the box which are screwed together with 14 mm long messing screws; the small plugs also made of Eccosorb which cover the screw holes underneath the bottom part; the central ring which is made of an Eccosorb MCS silicone rubber sheet; the PCB with the sample; the PCB cover; and the magnetic shield placed around the box. The next three sections will explain in detail the various components.

4.1 The Eccosorb

The microwave absorptive Eccosorb comes in two variations. Both are two part castable load absorbers and have the exact same electrical and magnetic properties.

The ECCOSORB CR-124 is the rigid type, a magnetically loaded epoxy. Once cured it is very hard, heavy and sticks strongly to most common surfaces, in particular metals. Once cured around the copper sampleholder, it cannot be removed. The types of materials one can use to make a mold for pouring this Eccosorb are thus extremely limited. One material to which it doesn't adhere strongly is Teflon (Polytetrafluoroethylene), which we chose to use for the molds.

The ECCOSORB CRS-124 is the rubber type, a magnetically loaded RTV silicone rubber. Once cured it is a true elastomer and adheres weakly to most surfaces. In particular, it releases easily from metals. The advantage is that we can remove the Eccosorb from the copper sampleholder at will.

The first experiment for T_1 and T_2 measurements had a protecting box built with the rubber Eccosorb, placed in the DR. In the end, following the warmup of the DR, it became apparent that the rubber Eccosorb hat entirely cracked and broken up, suggesting that it apparently doesn't withstand cryogenic temperatures. It is though explicitly specified in

Figure 4.1: (Top) The final Eccosorb box with the 8 microwave cables coming out on top and the three coil wires coming out on the bottom. (Bottom right) A close up view of the two-part box with the o-ring in between. (Bottom left) A photo of the Eccosorb as it is delivered in two parts, the epoxide"resin" in the metal can and the polyamine "hardener" in the small container.

its technical data sheet provided by the company: "when bonded to surfaces, ECCOSORB CRS will withstand temperature cycling (even to cryogenic temperatures)".

One possible explanation for the cracks could be the difference in the thermal expansion coefficient of copper and the rubber Eccosorb.

	Thermal expansion coefficient [m^3/K]
Copper	17 $\times 10^{-6}$
Rubber Eccosorb CRS	33 $\times 10^{-6}$

The rubber shrinks twice as quick as the copper during the cooldown of the DR, and therefore this might cause the rubber to crack open. A new box with the rigid Eccosorb CR was subsequently built and the same experiment was performed again, without cracking. For the rest of this thesis, all considerations are taken with the rigid ECCOSORB CR-124, unless otherwise specified.

We shall now address the question of how big and how thick this protecting box needs to be built. First, the magnetic shield has a diameter of 48 mm and the copper sample holder has a diameter 37 mm. This leaves a maximum of 4 mm lateral thickness of the Eccosorb

Figure 4.2: A photo of all the assembly components of the Eccosorb box when it is opened, and the magnetic shield into which the box is eventually placed in the DR.

around the sampleholder, see Fig. 4.3. The thickness is not limited underneath and on top of the sampleholder, where we chose 1 cm.

Does 4 mm thickness suffice to absorb the undesired radiation? The technical data sheet specifies the electrical and magnetic properties of the Eccosorb.

E-M properties of Eccosorb CR-124						
GHz	0.1	1.0	3.0	8.6	10.0	18.0
dB/cm	0.48	6.5	20	63	67	145

Table 4.1

Emerson&Cumming only specifies the E-M properties of the Eccosorb up to 18 GHz. A direct linear extrapolation from these given E-M properties values is shown in Fig. 4.4. One can expect that the absorption stays at least constant above 18 GHz. In the worst case, the attenuation constant is then 145 dB/cm. This attenuation is still by far sufficient for an Eccosorb layer of 4 mm.

4.2 Designing the molds and embedding the sampleholder into the epoxy

The Eccosorb box is made by placing the two parts of the sampleholder in two separate teflon molds and then pouring the prepared Eccosorb into the mold over the copper parts. After curing it, one must manage to take each half-box out of its mold without destroying the box nor the mold. Fig. 4.5 shows the two molds specifically designed for the sampleholder from Fig. 3.3 with the resulting two parts of the box.

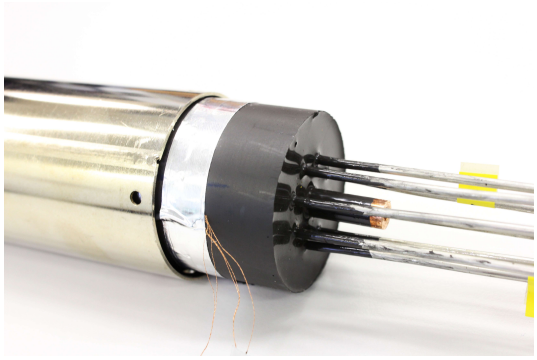

Figure 4.3: A photo of the Eccosorb box placed half-way inside the magnetic shield from the DR. The thickness of the box was chosen such that it fits with a 1.5 mm margin all around into the shield.

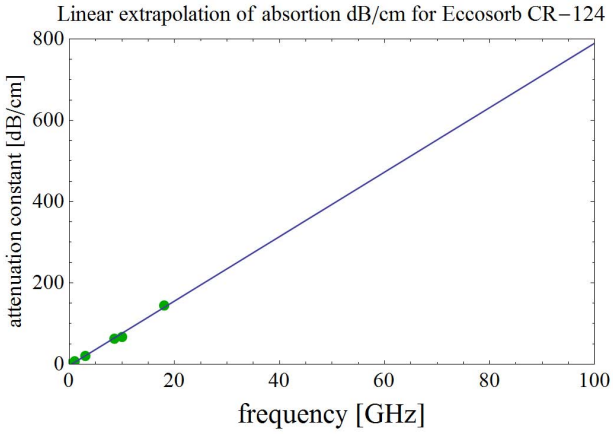

Figure 4.4: Linear extrapolation of the attenuation constant values known from the company specifications for the Eccosorb CR-124, as a function of radiation frequency up to 100 GHz.

Before describing how each of the two parts are constructed in detail, let's have a look at the procedure for pouring and curing the Eccosorb into the molds.

The procedure of the Eccosorb embedding

The Eccosorb is a two part castable magnetically loaded epoxy (polyepoxide, a thermosetting polymer) delivered in two containers, see Fig. 4.1(bottom left). Part A is the epoxide"resin" stored in the big metal can, and Part B is the polyamine "hardener" stored in the small container. When mixing these two compounds together, the amine groups react with the epoxide groups to form a covalent bond, creating the polyepoxide. A precise procedure must be followed for the epoxy to be correctly formed.

1. **Preparing**
   Part A is very viscous and cannot be extracted from its container without improving its pourability. Heating the entire can at 65°C for about 15-20 minutes renders it sufficiently pourable.

2. **Weigh out**
   Before mixing Part A with Part B, one must weigh them out with a ratio of 100/2.0. This means for each 100 g of Part A, take 2 g of Part B. For small quantities of epoxy it

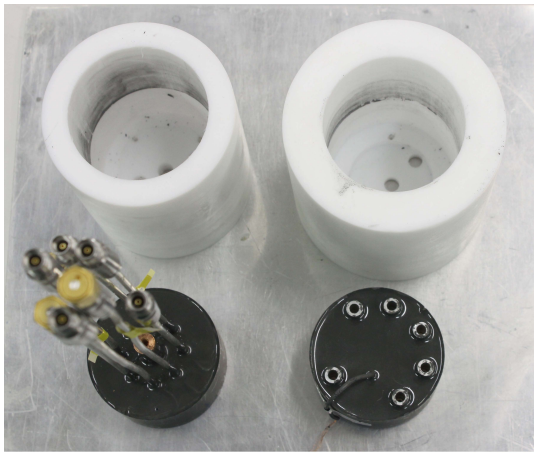

Figure 4.5: A photo of the two molds designed and fabricated to embedd the two parts of the Eccosorb box.

is thus very difficult to be precise with the amount of Part B taken. But it is extremely important to keep the weigh out ratio exact, or the polymerization process will not take effect correctly and the epoxy will not fully cure.

3. **Blending**
   Once the correct amounts of each part have been prepared, blend them together by stirring gently.

4. **Pouring**
   The epoxy is now ready to pour into the two molds. It is important that one acts very quickly up to this stage of the procedure, because the mixed epoxy cools down very quickly and turns very viscous, making it almost impossible to pour into the mold. This is why it is also helpful to heat the mold in advance.

5. **De-airing**
   Once the messy pouring is completed, one must remove all the air bubbles trapped in the mixture. This is achieved by placing the entire mold with the poured epoxy into a vacuum pump, proceeding to the so-called vacuum de-airing. Creating the vacuum and sucking out the entrapped air bubbles makes the entire poured epoxy inflate by double its size. For this reason, it is important that the height of the mold is at least twice as high as the amount of poured epoxy. Otherwise, the inflating epoxy overflows.

6. **Curing**
   Once all the bubbles are removed, the epoxy mixture needs to be cured according to the table below in order to become hard.

Temperature	Cure time
74°C	12 hours
93°C	4 hours
121°C	2 hours
149°C	1 hour

In particular, our Eccosorb box was cured at 74°C during 12 hours. Note that for the rubber Eccosorb CRS-124, the only difference in the procedure is that it cures at room temperature for about 12 hours.

After the cure, the epoxy is very hard and adheres weakly to the molds. Removing the box from the mold was done by hitting with a hammer all around the mold to release

the Eccosorb from the mold's walls. Then the box was pushed out by gently hitting from underneath on a small metal stick that fits through the holes drilled into the bottom of the mold (seen in Fig. 4.9). Notice that there are three drilled holes, one of which is placed in the center. This hole leads directly to the center of the surface of the copper middle piece from the sampleholder, as indicated in Fig. 4.6. This zone is very thin because the two small magnetic coils are placed in the cutout just underneath. So if one hits at that center spot, the thin copper breaks. Therefore, one must be careful and push out the box through the two other holes placed more to the side away from the center, where the copper piece is thick enough.

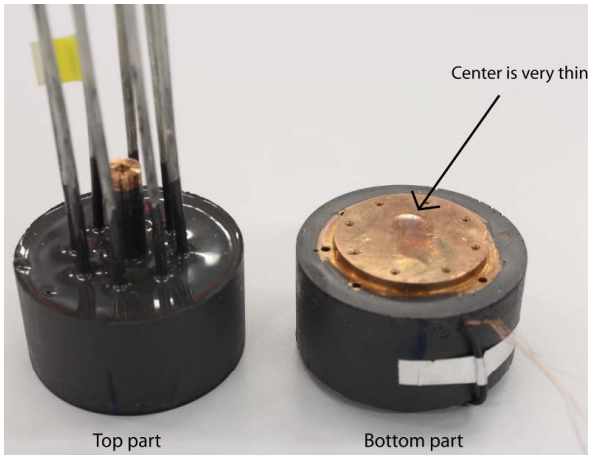

Figure 4.6: A photo of the two parts of the Eccosorb box, with the bottom part showing the very thin copper spot at the center of the middle lid.

In the next section, the detailed building of each half of the Eccosorb box before the embedding is described separately.

4.3 The Bottom and Top Part

4.3.1 The Top part and the coaxial cables

The top part of the Eccosorb box consists essentially of three components: the top lid of the sampleholder; eight coaxial RF cables screwed on it; and an extension screw holder which serves as a holder piece in the center for fixing the whole box in the DR. Fig. 4.7 shows how the top part construction is placed inside the mold before the embedding.

Figure 4.7: Bottom part prior to embedding.

The eight RF lines, leading ultimately to the the eight ports of the chip, must be assembled previously. The connectors on the side of the cables which attaches to the PCB are *SMP connectors* and the ones on the top end are *SMA connectors*. Assembling and soldering the connectors onto the coaxial cable is a standard procedure, described on the delivery package of the connectors. The company guarantees that all connectors have a maximum of about -19 dB reflection. However, there is a particular difficulty in assembling the SMP connectors, described in the following, which can lead to the cable having an increased reflection. The instructions to follow explain that one must leave a 0.3

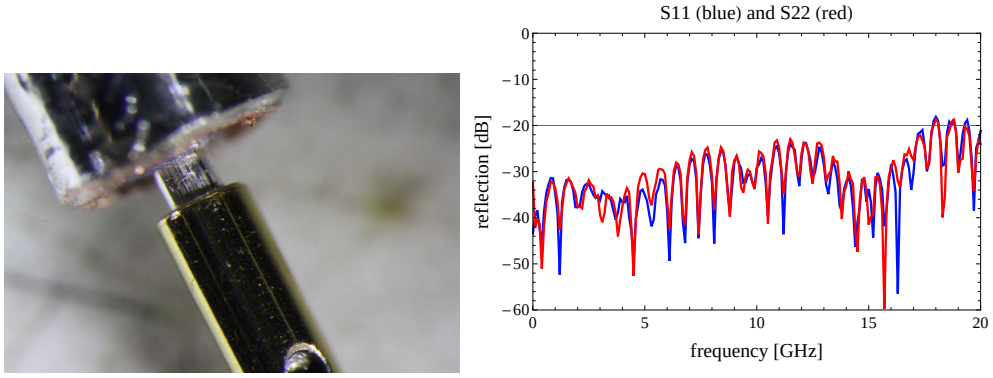

Figure 4.8: (Left) A close-up picture of the 0.3 mm gap that must be set between the SMP connector pin and the dielectric cutoff of the coaxial cable. (Right) The reflection coefficients S_{11} and S_{22} of one of the eight embedded cables connected to the PCB. The reflection is lower than -20 dB for all frequencies up to 18 GHz.

mm gap between the cut dielectric of the cable and the SMP pin (placed over the center pin of the cable), as shown in Fig. 4.8(left). The last step consists of placing the cover piece of the connector over this pin and soldering it to the cable's outer surface. The problem is that while soldering, the cable gets heated and therefore the dielectric inside expands substantially, up to several millimeters. As a consequence, the previously mentioned gap gets entirely covered by the dielectric. This fact leads to suboptimal impedance mismatches in the connectors and leads to high reflection. One solution to this problem is to heat the dielectric and cut the expanded part off before setting the pin and the desired gap. Following this method, all of our eight RF cables constructed achieve a maximal reflection of -23 dB below 18 GHz. Fig. 4.8(right) shows the reflection coefficients S_{11} and S_{22} of the S-matrix of one of the eight cables, measured with the network analyser.

4.3.2 The Bottom part

The bottom part of the Eccosorb box embeds the wires of the magnetic coils and the screws that tighten the closed box, showed in Fig. 4.9. The technical difficulty is being able to access the six screws after the embedding. For this issue we fixed with araldite glue an aluminium spacer tube of height 12 mm over each screw hole. It is important that there be sufficient tightening araldite glue around the spacer tubes on the copper lid, avoiding the liquid epoxy to flow into the tubes where the screws are tightened, as indicated by the red arrows in Fig. 4.9.

As previously shown in Fig. 3.3, the copper bottom lid and middle lid enclose the three magnetic coils, where the wires come out through the small center hole underneath the bottom lid. In principle, the wires could be embedded directly in the epoxy and stick out. However, for practical reasons, especially for the pouring and curing in the mold, the wires were directed through heat-shrinkable tubes. Note that the three coils built inside the bottom part cannot be exchanged. Special care should therefore be taken to the the wires coming out of the box, because they are thin and if they break off, the entire Eccosorb box becomes useless.

When finally screwing the bottom and top part of the Eccosorb box together, it must be ensured that the joint is tight to radiation as well. We use ECCOSORB MCS, a thin 0.5 mm, flexible, magnetically loaded, silicone rubber sheet, to make an o-ring placed and squeezed between the two parts (see 4.2 or Fig. 4.10). It is delivered as a sheet of 1 mm thickness though, so it must be abrased down to 0.5 mm, because this sheet is not flexible

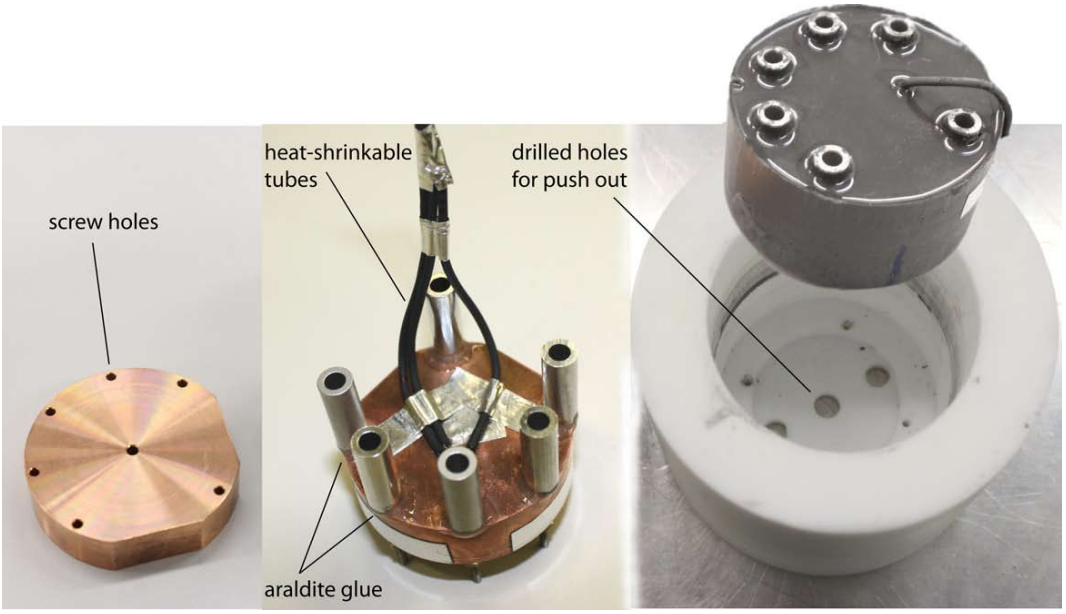

Figure 4.9: (Left) The bare bottom lid of the sampleholder. (Middle) The bottom part of the Eccosorb box prior to embedding. Aluminium tubes were glued to the lid to be able to access the screws even after the embedding. The heat shrinkable tubes protect the coil wires from the Eccosorb. (Right) The mold with the drilled holes at the bottom in order to be able to push out the box after the embedding.

enough and the screws would otherwise be too short.

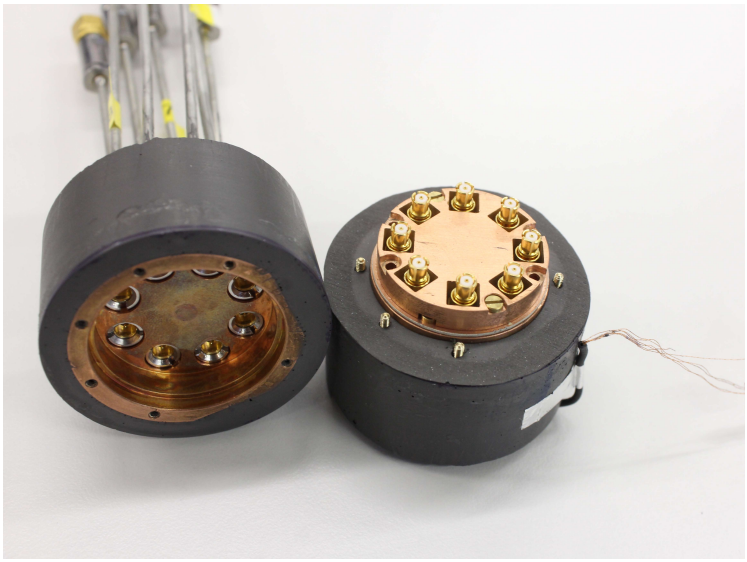

Figure 4.10: A photo of the two Eccosorb box parts, assembled and ready to close, and then set in the DR.

After assembling all the parts and closing the Eccosorb box, it was screwed by the extension screw holder onto the DR mixing chamber, the three outcoming coil wires were soldered to wires leading to the DC source, and six out of eight cables were connected to the RF lines leading to the microwave instruments.

Chapter 5

Measurements of decoherence

The goal of embedding the sampleholder into the absorptive Eccosorb medium is to test if the coherence times improve due to suppression of the external radiation from the DR. Since the T_1 and T_2 are expected to be frequency-dependant for the transmon, we measure the coherence times for various transition frequencies, starting at the sweet-spot and then gradually decreasing the frequency by tuning the qubit with the magnetic coils. The goal of this chapter is to present the results of T_1 and T_2 for different qubits for various frequencies. All measurements were performed twice with the Eccosorb. The first measurement set was performed with the rubber Eccosorb CRS box, which was cracked open the time during. A second measurement set was performed analog to the first one, but with the rigid Eccosorb box. Measuring the relaxation and dephasing of the qubit requires certain specific preliminary measurements each time, described in the beginning of this chapter. The first section describes how the sample is characterized through resonator and qubit spectroscopy, how the B-field matrix allowing for the tuning of the qubit to the different frequencies is determined, and how Rabi oscillations determine the pulse amplitude for excitation. The second section compares the T_2 and T_1 results for measurements performed first without any embedding, then with the broken Eccosorb box, and finally with the rigid Eccosorb box.

The sample has three qubits and three magnetic coils underneath it. A full control over all three qubit transition frequencies requires a B-field matrix of the three magnetic fluxes applied. In order to fully determine this matrix, the parameters for Eq.(2.19) must first be determined. The first subsection describes how to obtain the resonator frequency ω_{res} and Q-factor. Chapter 5 in [27] describes in detail how to find the Josephson energy E_J, the charging energy E_C, and the coupling strength g of the qubit.

5.1 Qubit spectroscopy and manipulation

5.1.1 Resonator spectroscopy

The resonator is a linear oscillator and therefore has a transmitted power which is determined by the Lorentzian

$$P(\nu) = P_0 \frac{\delta\nu_r^2}{(\nu - \nu_r)^2 + \delta\nu_r^2}, \tag{5.1}$$

centered around the resonance frequency ν_r with half width $\delta\nu_r$. The constant P_0 is the power transmitted through the resonator at the resonance frequency ν_r. To find the resonance frequency experimentally, we send a signal produced by the RF signal generator at a constant power of ≈ -25 dBm into the cavity and measure the transmitted power on the order of μW. By sweeping the frequency of the input signal, we obtain a peak in power transmission, as shown in Fig. 5.1a as an example of resonator spectroscopy. This particular data was taken on the resonator 3 of the cross cavity chip presented in chap. 6. From the

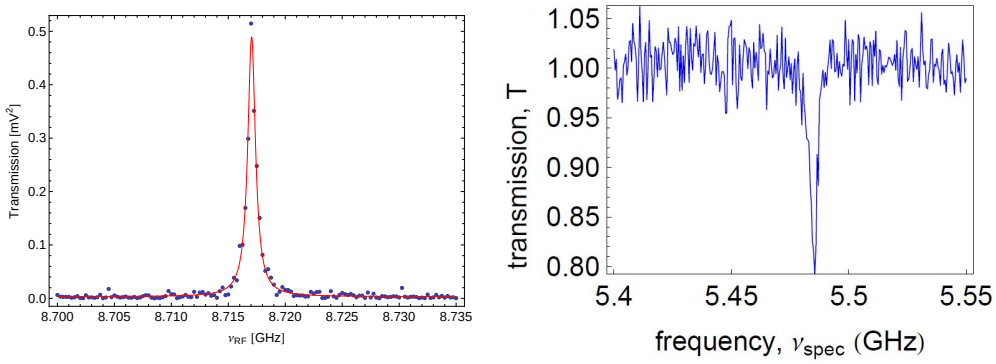

Figure 5.1: (Left) Resonator spectroscopy measurement and the fit. (Right) Qubit spectroscopy showing the transmission through the resonator sweeping the frequency. The dip in the transmission determines the qubit transition frequency.

Lorentzian fit of the data, the resonator frequency $\nu_r = \omega_r/2\pi = 8.717$ GHz is extracted, as well as a photon decay rate $\kappa/2\pi = 2\delta\nu_r = 0.818$ MHz, and a resulting quality factor $Q = \omega_r/\delta\nu_r = 10651$. The photons in this particular cavity thus bounce back and forth $Q/2\pi = 1700$ times between the two capacitors during the $T = 1/\kappa = 1.22$ μs they stay in the resonator.

5.1.2 Qubit spectroscopy

The qubit has a transition frequency corresponding to the energy level separation between the ground state and the first excited state, given by Eq.(2.19). For a given flux bias, the qubit frequency is measured by spectroscopy. Two microwave signals are applied. One continuous microwave tone is applied through the resonator at exactly its resonance frequency, assuring a high transmission. A second microwave drive is applied to the transmon via the gate line capacitively coupled to the island, and its frequency ν_{spec} is swept over a range which is far detuned from the resonator. As long as the drive frequency is different from the qubit transition frequency ν_{01}, the qubit stays in its ground state. However, when the drive frequency approaches ν_{01}, then the qubit acquires a population towards its excited state. From Eq. (2.27), the qubit state shifts the resonator frequency by the dispersive shift 2χ. Since the resonator is shifted, the continuous microwave tone applied to it has a decreased transmission amplitude. The drive frequency at the maximum drop in transmission is the qubit frequency $\omega_{01}/2\pi$, as shown in Fig. 5.1b, taken from [27] as an example.

5.1.3 The B-Field Matrix

From Eq.(2.19) we know that the qubit frequency has a periodic dependance on the magnetic flux bias voltage (the DC voltage applied to the coils). Consider each of the three coils $i = 1, 2, 3$ to have a bias voltage V_i. The magnetic flux resulting from a coil is linear in the voltage applied. Each of the three qubits $j = A, B, C$ feels a magnetic flux Φ_j which is a linear combination of the three separate magnetic fields, each produced by its V_i. Defining $\vec{\Phi} = (\Phi_A, \Phi_B, \Phi_C)$ and $\vec{V} = (V_1, V_2, V_3)$, we get the linear relation $\vec{\Phi} = \vec{\Phi}_{offset} + B\vec{V}$, where B is the 3×3 B-field matrix containing the flux period values for each of the three qubits for each coil separately, and $\vec{\Phi}_{offset}$ is the vector with its three components being the flux offset relative to each coil. In order to determine the B-field matrix experimentally, one needs to find the flux offset for each coil and the flux period for each of the three qubits for each of the three coils. For this task, we set the voltage of two coils to zero. Then we measure the qubit frequency by sweeping the bias voltage of the third coil. The resulting data shows the

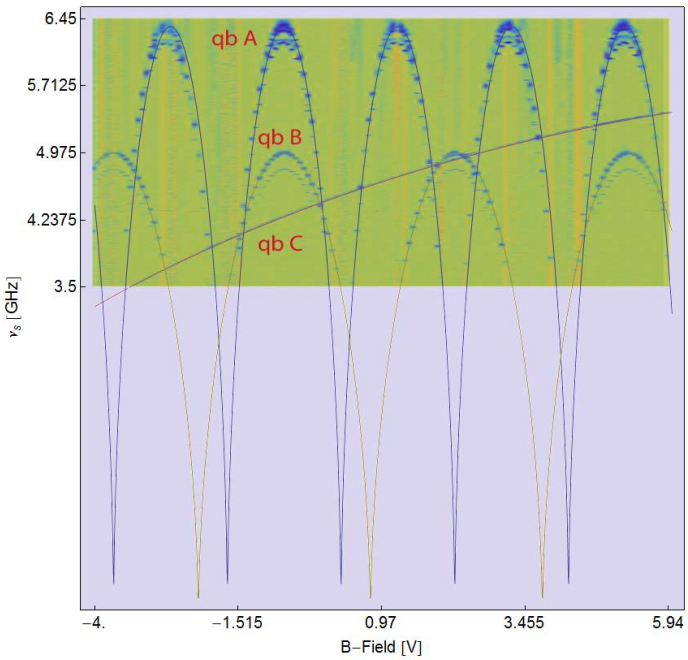

Figure 5.2: Spectroscopy measurement (blue points) sweeping the bias voltage (magnetic flux) of coil C, and the three fits for the three qubits. Fitting the data allows to determine the flux offset and the three flux periods for coil C.

dependance of each qubit on that single coil. The Fig. 5.2 shows the sweep of coil C (small coil) with the fit from which we extract the coil C period of each qubit and the coil C flux offset. Having fully determined the B-field matrix, we can now tune every qubit separately to any frequency. Additionally, the maximum frequencies of the qubits are given as the top point of the corresponding parabolas.

Recall from Fig. 3.1 that qubit A ($\nu_{maxA} = 6.714$) and qubit C ($\nu_{maxC} = 4.999$) are placed together on the right side of the chip, and qubit B ($\nu_{maxB} = 6.050$) is placed alone on the left side. Also, coil C is fixed on the copper middle lid directly underneath qubits A and C. This fact is now apparent in Fig. 5.2, where qubit B has obviously a very weak dependance on the bias voltage of coil C, since its period is enormous compared to the periods of the other two qubits.

5.1.4 Rabi oscillations

Qubit spectroscopy allowed us to find the transition frequency of the qubit ω_{01}. That known, one can coherently manipulate its state by applying microwave pulses at ω_{01} of various pulse duration and amplitudes. The interest is to perform quantum gates which rotate the Bloch vector on the Bloch sphere around the x or y axis via Eq. (2.24). For performing such a rotation on the state vector of the qubit, we need to know which amplitude the microwave pulse (with a fixed pulse duration of ∼10 ns) must have in order to get a rotation by a precise desired angle. Alternatively, one could set a fixed amplitude and vary the pulse duration. We drive the qubit through the gate line and use the resonator for the measurement pulse probing the state.

The Rabi measurement sequence is depicted in Fig. 5.3. The blue Gaussians represent the Rabi pulse sequence, where the amplitude of each subsequent pulse at ω_{01} is increased, starting from zero. After each pulse of the sequence, qubit spectroscopy is performed by applying a continuous measurement signal with a frequency ω_r resonant with the resonator,

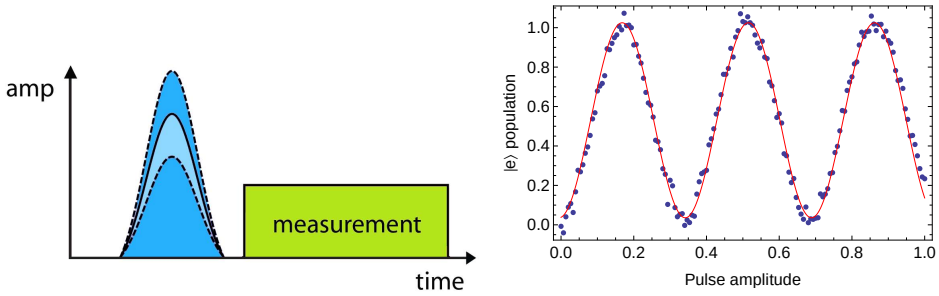

Figure 5.3: (Left) Pulse sequence for the determining the Rabi frequency. The pulse length is fixed while the amplitude is swept. (Right) Excited state population as a function of pulse amplitude. In this particular Rabi measurement, the extracted π-pulse amplitude is A_π=0.168 and the $\pi/2$-pulse amplitude is $A_\pi/2$=0.081.

acquiring thereby the excited state population. The measurement result of such a sequence is shown in Fig. 5.3. The population oscillates with the Rabi frequency as a function of the pulse amplitude of the qubit drive. After fitting the data, a pulse with the amplitude at which the population is at its maximum, i.e. which drives the qubit from the ground to the excited state, is called a π-pulse. Similarly, the one with half amplitude is called a $\pi/2$-pulse, which drives the qubit into an equal superposition state.

In the next two sections, for every measurement of decoherence there will first have been a Rabi measurement to calibrate the pulse amplitude needed for the excitations of the qubit into the desired states.

5.2 Measurements of decoherence times

This section presents the results of the dephasing T_2 and energy relaxation T_1 measurements at various qubit frequencies for the three different sampleholder situations: *without* an Eccosorb embedding, *with a broken* rubber Eccosorb box, and finally *with* the rigid Eccosorb embedding. For each of the two types of decoherence, the measurement method is first presented and then the results.

5.2.1 Ramsey fringes (T2)

The following method describes how the dephasing time of a qubit tuned to any frequency is measured. The qubit is initially considered in the ground state $|g\rangle$. A short microwave $\pi/2$-pulse at the qubit transition frequency ω_{01}, with phase $\phi = 0$ and with calibrated amplitude from the previously performed Rabi measurement, is applied to the qubit via its gate line. This brings the qubit into an equal superposition state. Then, after a time delay of Δt, another same $\pi/2$-pulse is applied (see Fig. 5.4a). Consider the experiment to be in the frame rotating with the frequency of the drive. If the drive is at the same frequency as the qubit, i.e. the detuning $\Delta_d = \omega_r - \omega_{01} = 0$, then the qubit state will not acquire a phase during the time interval Δt between the two pulses, i.e. the Bloch vector doesn't precess around the z-axis. Therefore the second $\pi/2$-pulse brings the qubit into the excited state, adding up to the first pulse and achieving an overall π-pulse performed on the qubit. However, for the Ramsey experiment, we detune the drive on purpose, setting it off-resonant by $\sim \Delta_d = 4$ MHz. Therefore, in the rotating frame, the qubit acquires a phase $\phi = \Delta_d \Delta t$ during the delay time by rotating around the z-axis. When the second $\pi/2$-pulse is then applied, the final state has a projection on the z-axis which is dependant on the accumulated phase: the x-component of the state is either rotated towards the excited state ($+z$) or the

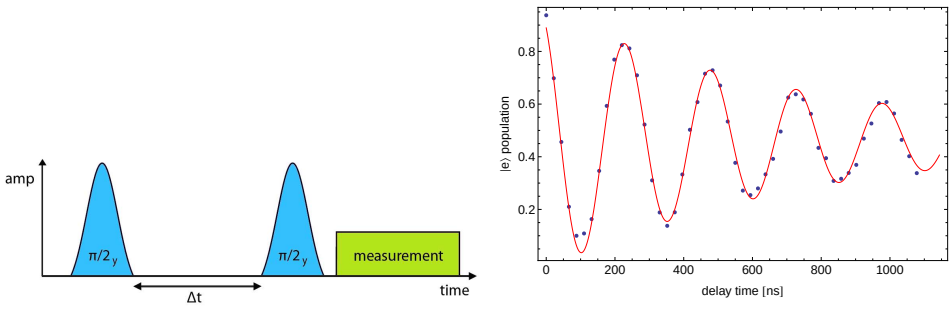

Figure 5.4: (Left) Schematic representation of a Ramsey pulse sequence. The delay time Δt between the two $\pi/2$-pulses is increased in steps of 30 ns. (Right) Excited state population as a function of the time delay between the Ramsey pulses. The Ramsey interference fringes are due to the small off-resonance of the qubit drive. Dephasing is responsable for the exponential decay. Fitting the decay gives the T_2.

ground state ($-$z). Hence it ultimately has a sinusoidal dependance on the delay time. Finally, after the second pulse, the qubit state population is read out through the resonator.

The whole pattern just described is repeated by sweeping the delay time Δt from 0 to $\sim$ 1500 ns in 50 steps of 30 ns, The whole experiment is repeated and averaged over 6.5×10^4 times. An example of such a Ramsey experiment is shown in Fig. 5.4b. The oscillations follow an exponential decay law. The envelope of the fitted data gives the exponential dephasing rate T_2. In this particular example measured on the cross-cavity chip (c.f. chap. 6), the extracted dephasing time is T_2= 771 ns with a detuning frequency Δ_d= 4.003 MHz.

The goal of the Eccosorb box is to test if the embedding improves coherence times of the qubits A, B, and C of our sample at various transition frequencies. The dephasing results are presented here, and the relaxation results are presented in the next subsection. For qubit A of our three-qubit sample, the results are shown in Fig. 5.5. The T_2 was measured sweeping the qubit frequency from 3.5 to 7 GHz, and was done for all three cases: without-, with broken-, and with Eccosorb. Qubits B and C were parked at their sweet spot the time being. Recall that the resonator frequency is much higher than the max frequencies of the three qubits. This makes experiment easier, because we do not have to worry about the qubit crossing the resonator during the qubit frequency sweep.

Note that the measurements without the Eccosorb embedding (shown in green) were performed by hand. This means that it not only takes a lot of time, but that for each T_2 data point one must first set the coil bias voltage to the predicted value that tunes the qubit to the desired frequency; then find the resonance frequency with resonator spectroscopy; find the transition frequency with qubit spectroscopy; use these values to perform Rabi oscillations to get the π- and $\pi/2$-pulse amplitudes; insert these values into the Ramsey pulses pattern files; perform the Ramsey measurement, analyse the data and finally extract the T_2 value from the exponential fit. On the other hand, the measurements with the broken Eccosorb as well the ones with the rigid Eccosorb embedding were performed using an automatic LabVIEW VI program (named "Tracker") which executes the above described procedure on its own. The problem with the tracker is that he does not notice on his own when the Rabi fits are "bad". Therefore many T_2 data points are worthless because their Ramsey sequence was executed with wrong pulse amplitude or off resonance. Also, at some qubit frequencies, obvious beating is present in the Ramsey oscillations. The beating is presumably due to some defects or to two-level fluctuators in the vicinity of the qubit transition frequency. All these "bad" points were eliminated by hand in the end.

The results for the three cases in Fig. 5.5 show that the Eccosorb embedding for our transmon did not improve the dephasing time. Moreover, the blue data points show that

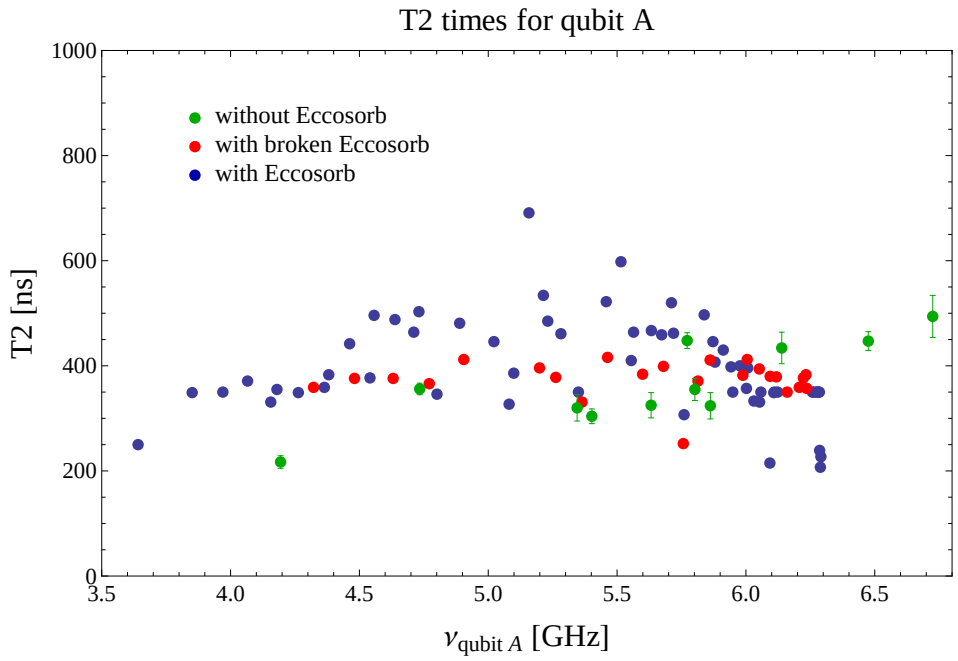

Figure 5.5: T_2 measurement results of qubit A varying the transition frequency between 3.5 to 7 GHz. The green points are the data measured by hand prior to the embedding. The red and blue points were measured with the "Tracker" respectively with the broken rubber Eccosorb and the rigid Eccosorb. The error bars are errors on the exponential data fit.

the dephasing time measurements around a similar frequency can be widespread over almost 300 ns. This makes it difficult to notice any dependency trend of T_2 on frequency in such a short sweep range.

5.2.2 Qubit relaxation time (T1)

The energy relaxation time T_1 is measured by extracting the exponential decay of the qubit population, selon $p(t) = e^{-t/T_1}$. The Fig. 5.6a represents the pulse sequence schematically. A resonant π-pulse is applied to excite the qubit. After waiting a time Δt the remaining population is measured by the usual readout through the resonator. Sweeping the delay time Δt from 0 to 3500 ns, the remaining population decreases exponentially with every step. Each step is measured and averaged over 10^4 times, and each sequence is performed and averaged over 6.5×10^4 times. The Fig. 5.6b shows an example of data measured on the cross-cavity chip with an extracted energy decay time $T_1 = 3.526$ μs.

For qubit A of our three-qubits sample, the T_1 results are shown in Fig. 5.7, where the frequency was swept again from 3.5 to 7 GHz for all three cases. The green points were performed by hand and the red and blue with the Tracker, analog to the T_2 case. We can clearly conclude that the Eccosorb embedding does not improve the relaxation time of our transmon, since the blue data points are on average not higher than the green and red ones. At the higher frequencies it seems that the T_1 even decreased slightly, but we cannot make a correlation with the embedding, since this could be due to many other reasons (different cooldown, nearby resonances, etc.). However, we can clearly observe a dependence that T_1 increases with decreasing transition frequency, starting at $\sim$ 700 ns at 6.2 GHz and rising to $\sim$ 1300 ns at 4.0 GHz. This dependency will be investigated further in chap. 6.

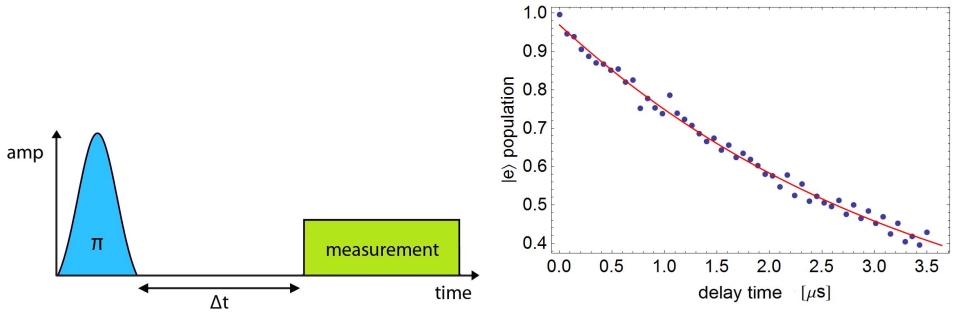

Figure 5.6: (Left) Schematic reprentation of the energy relaxation measurment pulse sequence. The amplitude of the π-pulse is fixed while the delay time is swept. (Right) Excited state population as a function of the delay time. From the exponential fit one determines the T_1.

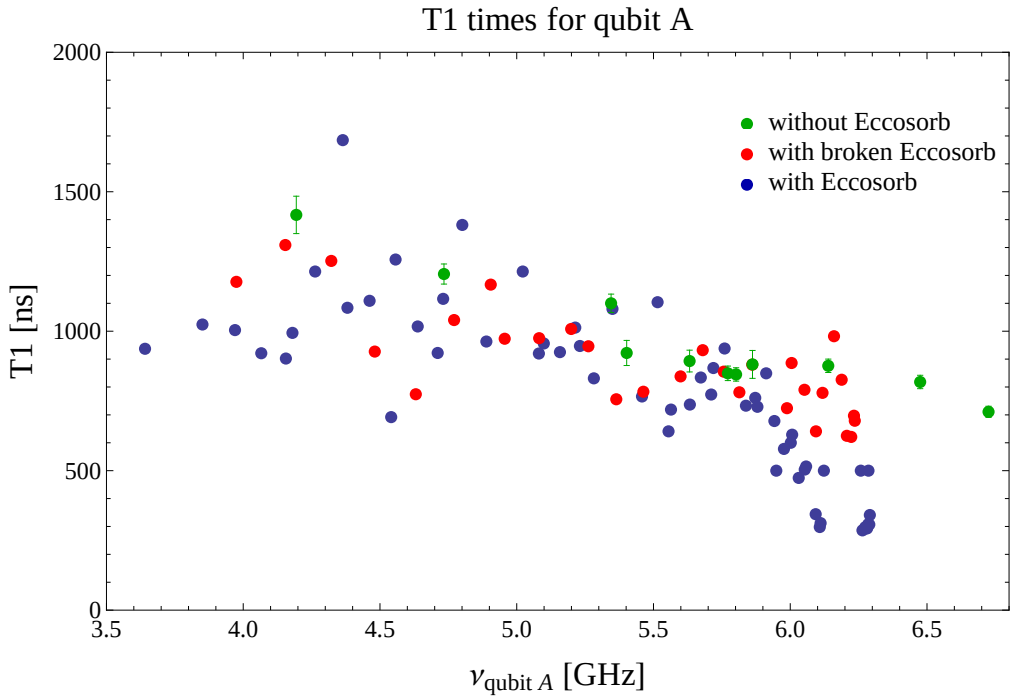

Figure 5.7: T_1 measurement results of qubit A varying the transition frequency between 3.5 to 7 GHz. The green points are the data measured by hand prior to the embedding. The red and blue points were measured with the "Tracker" respectively with the broken rubber Eccosorb and the rigid Eccosorb. The error bars are errors on the exponential data fit.

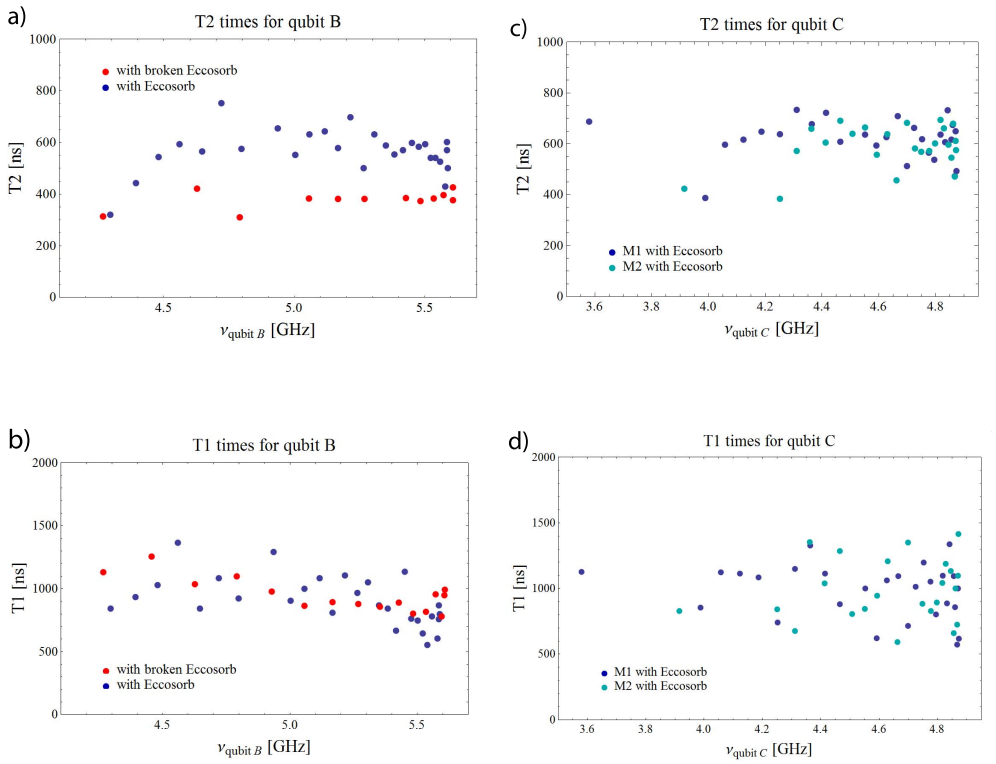

Figure 5.8: a) T_2 and b) T_1 measurement results for qubit B. The red points were performed with the broken rubber Eccosorb embedding and the blue points with the rigid Eccosorb. c) T_2 and d) T_1 measurement results for qubit C. Both were performed with the rigid Eccosorb embedding, but twice with a day interval, represented by the two different colours light and dark blue.

The decoherence measurements for qubits B and C are presented in Fig. 5.8. For the qubit B, only the cases with broken- and with rigid Eccosorb were measured. We can observe a small improvement in T_2 by ∼200 ns on average across the sweep. However, this small increase could also be attributed to the fact that the two measurements were performed in two different cooldowns of the fridge. It is a known fact from experience that our decay times may change by an amount on the order of 25% from cooldown to cooldown. We therefore don't assign such an insignificant improvement to any effect of the Eccosorb embedding.

The qubit B results for T_1 confirm that the embedding doesn't have any effect on the relaxation of our transmons. It also brings forth the same dependency of T_1 on the frequency as for qubit A, even though the slope is much flatter.

For qubit C, only the case with the rigid Eccosorb was measured for dephasing and relaxation, but it was performed two times with a day interval, represented by the two colors in Fig. 5.8c and d. From this plot we simply infer that the results are reproducible, that they can be widespread, and that one needs a much larger data range to notice any dependencies.

In end, the question now arises: why has the relaxation time of the IBM Group's qubit significantly increased by the embedding in an absorptive medium and ours hasn't? There could be several reasons for this. First, the IBM Group operates a capacitively shunted flux qubit, whereas we operate a superconducting charge qubit. These two qubits could be subject to different phenomena at this stage, where theirs suffered from quasiparticles generated by external radiation and ours is first limited by some other mechanism [30].

The second reason is that their flux qubit was not previously placed inside a copper sam-

pleholder like ours. Thus the external radiation generating the quasiparticles was limiting their unprotected flux qubit's decay time. In contrast, for our charge qubit the radiation may already have mostly been absorbed by our sampleholder, rendering the Eccosorb superfluous. Furthermore, we cannot exclude the possibility that the quasiparticle generation by external radiation is actually present, but the charge qubit is currently limited by another mechanism, such that it may start only at a later stage (higher T_1's) to be limited by the quasiparticle generation, at which the Eccosorb would then maybe begin to take effect.

Chapter 6

Cross-cavity chip

As the investigations to discover the decoherence mechanisms in the transmon continue, the idea came up to try reducing the relevant electric fields in order for charge noise to diminish, which in turn would maybe increase the coherence times. For this effect a new chip was fabricated with slightly increased capacitor gaps in the transmon qubits, thereby decreasing the electric field intensity between the capacitor plates. The first section of this chapter introduces this new cross-cavity chip. The second section presents T_1 and T_2 measurements for this sample and the third section establishes a theoretical model possibly describing the frequency dependence of the relaxation.

6.1 Four qubits, three resonators

In Fig. 6.1 the design of the cross-cavity sample is shown with its three resonators and four qubits (dark green). All four qubits have the same size and geometry, with the exception that qubits 2 and 3 have their finger capacitor in an "L" shape. An optical microscope picture of qubits 3 and 4 and a close up view of their split Josephson junctions is shown in Fig. 6.2. The qubit geometry differs mainly from our previous 3-qubit 1-resonator sample showed in Fig. 3.1 by the fact that the finger capacitors are rounded instead of squared and that the size of the finger capacitor gap is increased by ~ 8 μm. The idea behind this change is that a bigger capacitor gap leads to a weaker electric field between the capacitor plates. Weaker electric fields lead to less charge noise, which in turn should allow for higher relaxation times. The measurements for this sake are presented in the next section.

The characteristic properties of qubits 3 and 4 are shown in the table below. The resonator 3, which is coupled capacitively with the qubits 3 and 4, has a resonance frequency of ~ 8.516 GHz when the qubits are at their sweet spot, and has a quality factor $Q = 10000$.

	ν^{max} [GHz]	$E_C/\hbar$ [GHz]	$g/2\pi$ [MHz]
Qubit 3	9.655	0.295	318
Qubit 4	9.411	0.331	334

The new cross-cavity chip has now 16 ports, 2 for each resonator (res 2 is disconnected to input and output ports in this particular sample though), and 2 or 3 for each qubit (charge and flux line). Therefore the PCB and the sampleholder must be adapted in size. The 16-port PCB is depicted in Fig. 6.3. In order to control the tuning of each of the four qubits individually, one would need four magnetic coils underneath the PCB. Our 16-port sampleholder is currently only designed for three coils, the same three as in the previous 8-port sampleholder. This is sufficient for this thesis though, since we only measured coherence

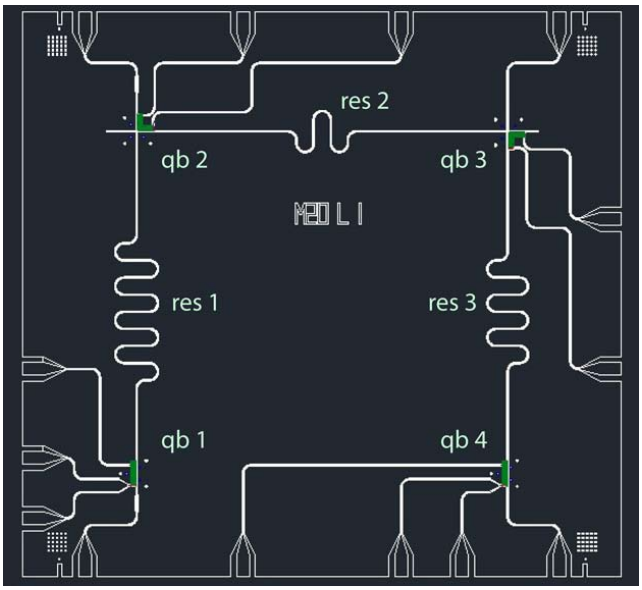

Figure 6.1: Cross-cavity chip design by Yulin Liu. One recognises the three resonators crossing each other. The crossing is implemented by means of aluminium air bridges. Note that res 2 is open ended and is not connected to the PCB. The four qubits are placed respectively at the intersections of the three resonators.

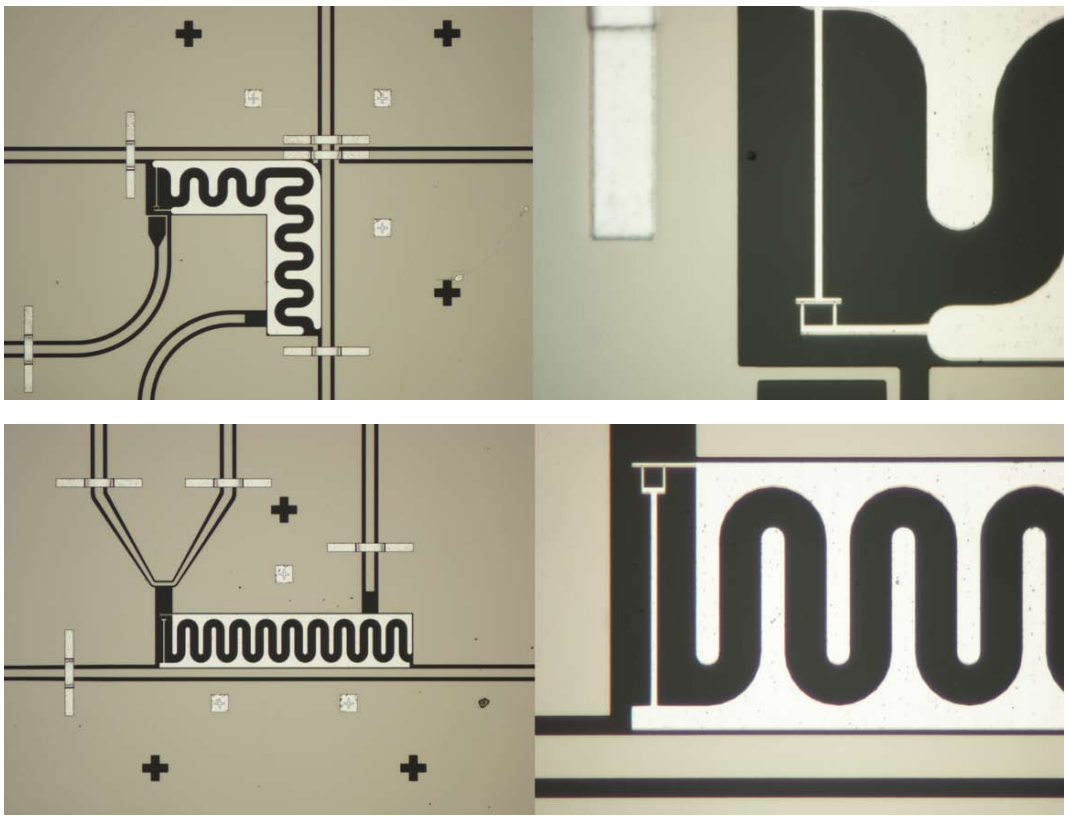

Figure 6.2: Optical microscope pictures of the"L"-shaped qubit 3 (top) and a zoom on its split Josephson junction, and of qubit 4 (bottom) and its junction. One can now observe the air bridges of the resonator crossing.

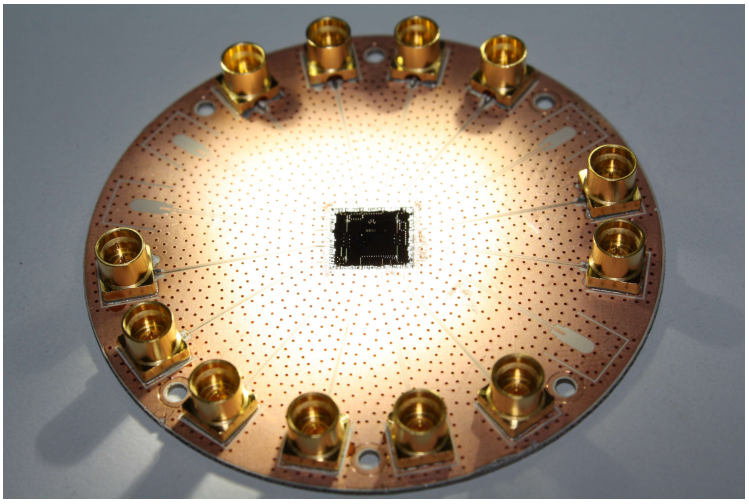

Figure 6.3: Photo of the 16-port PCB with the integrated cross-cavity sample.

times for one qubit, namely qubit 4.

6.2 Measurements of decoherence reloaded

Measurements of T_2 and T_1 were performed on qubit 4 in resonator 3 of the cross-cavity chip in a similar manner as with the previous 8-port sample. The only difference is that the now 16-port sampleholder is not embedded in any kind of Eccosorb and the measurements were performed by hand. Note also that the maximum frequencies of the qubits ($\sim$ 9.5 GHz) are now above the resonator frequency ($\sim$ 8.6 GHz). The frequency sweep was therefore done from 4 GHz up to only 7.3 GHz, hence avoiding any crossing with the resonator.

The Fig. 6.4 and Fig. 6.5 show the results of T_2 and T_1 for qubit 4 (purple data) of the cross-cavity sample (no Eccosorb), compared to those of qubit A from the 8-port sample without Eccosorb of the previous chapter (green data). The qubit 3 which is also placed on the resonator 3 was tuned and parked under 4 GHz during the experiment.

From these results the first conclusion is that the coherence times have improved by an average factor of $\sim$ 2 times for T_2 and $\sim$ 3 times for T_1 over the whole frequency sweep, presumably due to the increase in the finger capacitor gap. The highest relaxation time obtained is $T_1 = 4.723$ μs at $\nu_{qb4} = 4.621$ GHz, and the highest dephasing time is $T_2 = 966$ ns at $\nu_{qb4} = 7.32$ GHz. The second conclusion is that the dephasing time decreases with decreasing frequency and that relaxation time increases with decreasing frequency. It is however difficult to recognize if the dependance is linear or quadratic, because the data range is too small. The next section will analyse this in more detail for T_1. For the T_2, recall that the change in qubit frequency due to fluctuations in the external applied magnetic field is larger when the qubit is at lower frequencies, i.e. $\partial\omega/\partial\Phi$ is bigger (c.f. Fig. 5.2). Since it is the longitudinal noise that cause dephasing, as for example the magnetic fluctuations, it is expected that the T_2 is proportional to the qubit frequency.

Note the three additional points in the T_1 plot figure. One relaxation point (light blue) was measured on qubit 1 in resonator 1 of the current cross-cavity chip to check that the order of magnitude of T_1 is consistent across several qubits. In addition, the figure shows two points (orange and brown) that were measured separately on a cross-cavity sample that had been previously fabricated. This previous sample had the particularity that it additionally had an increased capacitor gap between the transmon island and the resonator. We observe that those qubits also have a consistent improved T_1 value at $\sim$ 5 GHz in comparison to

this sample.

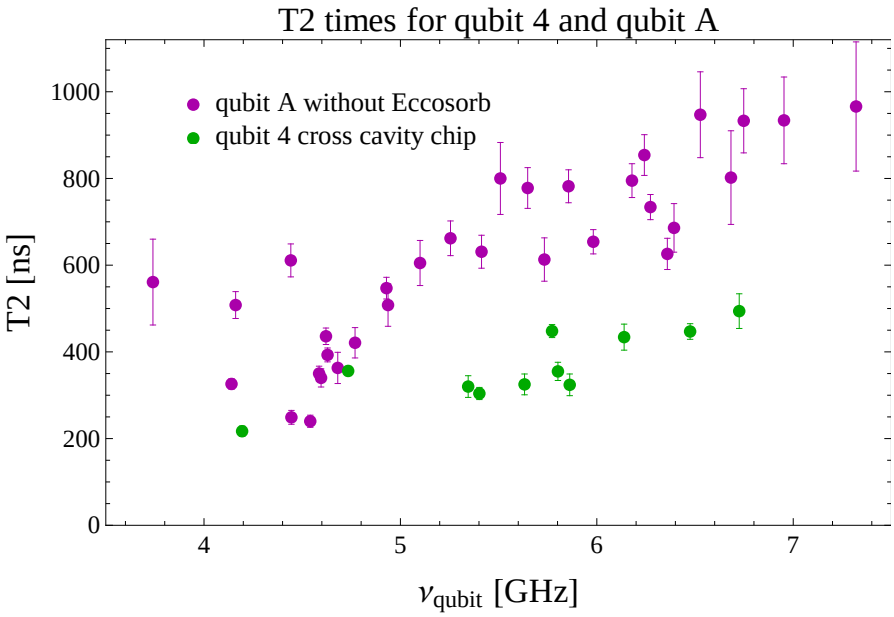

Figure 6.4: T_2 measurement results for qubit 4 (purple) of the cross-cavity sample compared to the results of qubit A (green)from the 8-port sample without Eccosorb, varying the qubit frequencies from 3.5 to 7.3 GHz.

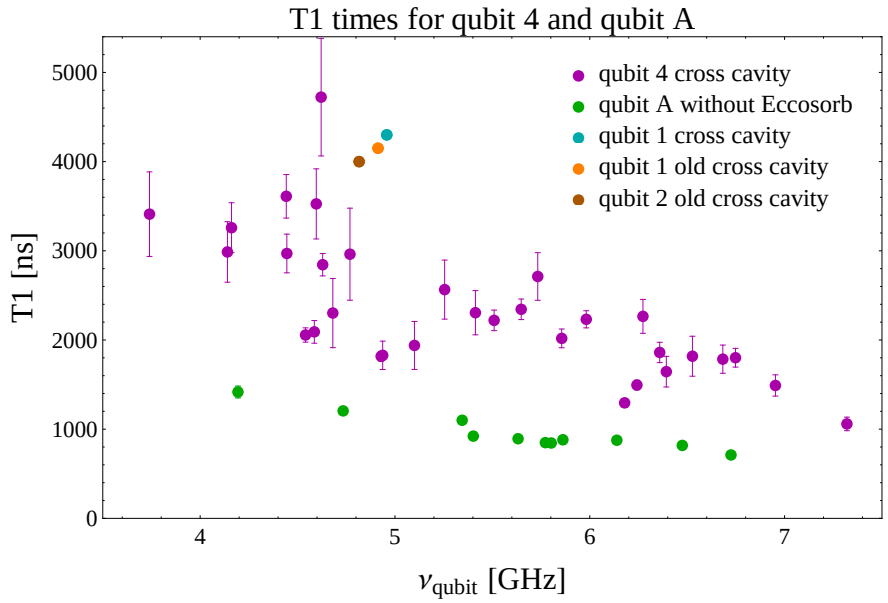

Figure 6.5: T_1 measurement results for qubit 4 (purple) of the cross-cavity sample compared to the results of qubit A (green) from the 8-port sample without Eccosorb. The additional blue point was measured for qubit 1, and two single points (orange and brown) were measured separately on a previously fabricated cross-cavity sample.

6.3 A sub-ohmic bath model

The results in Fig. 6.5 showed us a significant improvement in the relaxation time for the qubits with increased finger capacitor gaps. This fact suggests that the noise source presumably causing the relaxation is related to the intensity of the electric fields in the transmon, hence due to on-chip charge noise. In this section, we present a model for a general noise bath and consider the sub-ohmic case to fit our data.

Current noise and decoherence theory is not capable of describing the noise sources with a detailed microscopic model, but often the environment can be sufficiently modelled by a bath of harmonic oscillators with frequency spectrum adjusted to reproduce the observed power spectrum [31]. Recall the Hamiltonian (2.14) of the Cooper pair box

$$\mathcal{H}_{CPB} = \frac{(2e)^2}{2C_\Sigma}\left(\hat{N} - \frac{V_g C_g}{2e}\right)^2 - E_J \cos\hat{\delta}, \tag{6.1}$$

with $C_\Sigma = C_g + C_J$ the total capacitance.

We consider the source of decoherence as a bath of harmonic oscillators which can be modeled by an effective impedance $Z(\omega)$, placed in series with the voltage source V_g (of the CPB circuit), and producing a fluctuating voltage δV. Expanding the Hamiltonian (6.2) with $V_g \to V_g + \delta V$ gives

$$\mathcal{H} = 4E_C\left(\hat{N} - \frac{V_g C_g}{2e}\right)^2 + 2e\hat{N}\frac{C_g}{C_\Sigma}\,\delta V - E_J\cos\hat{\delta}, \tag{6.2}$$

where the second term is now seen as the perturbation contribution $\mathcal{H}_{\delta V}$ to the Hamiltonian by the noise bath. Its matrix elements are

$$\langle i|\,\mathcal{H}_{\delta V}\,|j\rangle = 2e\frac{C_g}{C_\Sigma}\delta V\,\langle i|\,\hat{N}\,|j\rangle\,. \tag{6.3}$$

From [17] chap. III, we have the number operator $\hat{N}$ for our transmon taking the form $\hat{N} = -i(E_J/8E_C)^{1/4}(\hat{b} - \hat{b}^\dagger)/\sqrt{2}$, so that

$$|\,\langle j+1|\,\hat{N}\,|j\rangle\,| \approx \sqrt{\frac{j+1}{2}}\left(\frac{E_J}{8E_C}\right)^{1/4}. \tag{6.4}$$

Furthermore, with $\hat{b}$, $\hat{b}^\dagger$ being the annihilation and creation operators for the harmonic oscillator approximating the transmon,

$$|\,\langle j+k|\,\hat{N}\,|j\rangle\,| \xrightarrow{E_J/E_C\to\infty} 0 \tag{6.5}$$

with $|k| > 1$. Since the transmon has a large E_J/E_C, this shows that there is negligibly week coupling for higher transitions than $|j\rangle$ to $|j+1\rangle$. For our two-level system with $j = 0$ and the diagonal elements $\langle 0|\,\hat{N}\,|0\rangle = \langle 1|\,\hat{N}\,|1\rangle = 0$, we obtain

$$\hat{N} = \frac{1}{\sqrt{2}}\left(\frac{E_J}{8E_C}\right)^{1/4}\sigma_y, \tag{6.6}$$

giving the Hamiltonian

$$\mathcal{H}_{\delta V} = \sqrt{2}e\frac{C_g}{C_\Sigma}\left(\frac{E_J}{8E_C}\right)^{1/4}\delta V\,\sigma_y. \tag{6.7}$$

Comparing this with the general Hamiltonian form of a transverse noisy variable δV with coupling g

$$\mathcal{H} = \frac{1}{2}\,g\,\delta V\,\sigma_y, \tag{6.8}$$

we obtain the value of the coupling strength of our noise

$$g(\omega) = 2\sqrt{2}\, e\, \frac{C_g}{C_\Sigma} \left(\frac{E_J}{8E_C}\right)^{1/4} = 2\sqrt{2}\, e\, \frac{C_g}{C_\Sigma} \left(\frac{\hbar\omega + E_C}{8E_C}\right)^{1/2}. \tag{6.9}$$

The last equality is achieved by inverting the Eq. (2.19). So the coupling is proportional to the square root of the qubit frequency.

The relaxation rate of the qubit $\Gamma_1 = \Gamma_{|1\rangle\to|0\rangle} + \Gamma_{|0\rangle\to|1\rangle}$ due to our noise bath is calculated with Fermi's Golden Rule. For the relaxation rate $\Gamma_{|1\rangle\to|0\rangle}$ we have

$$\begin{aligned}
\Gamma_{|1\rangle\to|0\rangle} &= \frac{2\pi}{\hbar}\frac{|g(\omega)|^2}{4}\sum_{i,f}\rho_i |\langle i|\,\delta V\,|f\rangle|^2\,\delta(E_i + \Delta E - E_f) \\
&= \frac{2\pi}{\hbar}\frac{|g(\omega)|^2}{4}\sum_{i,f}\rho_i \langle i|\,\delta V\,|f\rangle\langle f|\,\delta V\,|i\rangle \frac{1}{2\pi\hbar}\int dt\, e^{i\frac{t}{\hbar}(E_i+\Delta E-E_f)} \\
&= \frac{|g(\omega)|^2}{4\hbar^2}\int dt \sum_i \rho_i \langle i|\,\delta V(t)\,\delta V\,|i\rangle\, e^{i\frac{t}{\hbar}\Delta E} \\
&= \frac{|g(\omega)|^2}{4\hbar^2}\langle \delta V^2_{\omega=\Delta E/\hbar}\rangle.
\end{aligned} \tag{6.10}$$

The kets $|i\rangle$ and $|f\rangle$ are the initial and final states of the bath. The probability density ρ_i is the probability for the bath to be in the initial state $|i\rangle$. For the excitation rate $\Gamma_{|0\rangle\to|1\rangle}$ we get

$$\Gamma_{|0\rangle\to|1\rangle} = \frac{|g(\omega)|^2}{4\hbar^2}\langle \delta V^2_{\omega=-\Delta E/\hbar}\rangle. \tag{6.11}$$

Since the power spectrum of the perturbation field δV is defined as

$$S_{\delta V}(\omega) = \frac{1}{2}\int dt\, e^{i\omega t}\langle\{\delta V(t), \delta V(0)\}\rangle, \tag{6.12}$$

we get the relaxation time

$$\frac{1}{T_1} = \Gamma_1 = \frac{|g(\omega)|^2}{2\hbar^2} S_{\delta V}(\omega = \Delta E/\hbar). \tag{6.13}$$

In the present case of the transmon considering the bath as voltage fluctuations modeled by the impedance $Z(\omega)$ in series, the fluctuation-dissipation theorem gives

$$S_{\delta V}(\omega) = Re[Z(\omega)]\,\hbar\omega\coth\left(\frac{\hbar\omega}{2k_BT}\right). \tag{6.14}$$

Recall the behavior of the function

$$\coth\left(\frac{\hbar\omega}{2k_BT}\right) = \begin{cases} 1 & \text{if } \hbar\omega \gg k_BT \\ \frac{2k_BT}{\hbar\omega} & \text{if } \hbar\omega \ll k_BT \end{cases} \tag{6.15}$$

In our experiments the transmon is operated in the case $\hbar\omega \gg k_BT$. Setting (6.9) and (6.14) for this case into (6.13), we get a relaxation rate

$$\Gamma_1 \begin{cases} \propto \omega^2 & \text{if } Re[Z(\omega)] = R \quad \to \quad \text{Ohmic case} \\ \propto \omega & \text{if } Re[Z(\omega)] = \frac{A}{|\omega|} \quad \to \quad \text{Sub-ohmic case} \end{cases} \tag{6.16}$$

As it is observed in the results from Fig. 6.5, our data on T_1 seems to show either a $1/\omega$ (Ohmic) or $1/\omega^2$ (Sub-ohmic) dependency, and it is close to impossible to determine from the short range of data which one of these two it really is. Despite this difficulty, [31]

states that there have been several experiments with Josephson circuits that revealed in the low-frequency range the presence of 1/f noise. It appears that frequently it arises from "background charge fluctuations", or so-called "two-level fluctuators" (TLF), which would give a noise power spectrum

$$S_{1/f}(\omega) = \frac{\alpha_{1/f}}{C_g^2}\frac{e^2}{|\omega|}. \tag{6.17}$$

As cited in [31], recent experiments from [32] yield a strength of dissipation $\alpha_{1/f} \sim 10^{-7} - 10^{-6}$ and "indicate that the 1/f frequency dependence may extend up to high values, of the order of the level spacing" of the qubit. In the following, we will fit our data to this type of 1/f noise power spectrum and see what value of $\alpha_{1/f}$ we obtain for our system.

We must first find the above introduced constant A for the Sub-ohmic case. Consider our general power spectrum $S_{\delta V}(\omega)$ in Eq. (6.14) for low-frequencies $\omega \to 0$ and the Sub-ohmic case in (6.16). Then we have $S_{\delta V}(\omega \to 0) = A\, 2\, k_B\, T/|\omega|$. Comparing this to the 1/f noise power spectrum in (6.17), we obtain $A = \alpha_{1/f}\, e^2 \,/\, C_g^2\, 2\, k_B\, T$. We can now go back to Eq. (6.13) and plugin the expression for A and for $g(\omega)$, the power spectrum being in the Sub-ohmic case with $\hbar\omega \gg k_B T$. This gives finally the relaxation rate

$$\begin{aligned} T_1^{-1} = \Gamma_1 &= \frac{1}{2\hbar^2}|g(\omega)|^2\, \hbar A \\ &= \alpha_{1/f}\, \omega\, \frac{E_C}{k_B T} \end{aligned} \tag{6.18}$$

We now plot this linear decay rate with parameters in Table **??** and fit it to the qubit 4 data by choosing the parameter $\alpha_{1/f}$.

T	25×10^{-3} [K]
E_C	$2\pi\hbar\ 300 \times 10^6$ [J]
C_g	2×10^{-15} [F]
$\alpha_{1/f}$	3.45×10^{-6}

The plot of T_1 from Eq. (6.18) with the values in the table is shown in blue in Fig. 6.6a. The blue plot in Fig. 6.6b shows the same for the decay rate, which is just the inverse, but is easier to visualize because it has the linear dependence. The green plot shown in both figures is simply a quadratic best fit of the purple data points. It is again obvious that it is difficult to judge if the linear or the quadratic dependence fits the data better because of the limited data range. The point of the above approach is that by choosing an $\alpha_{1/f} = 3.45 \times 10^{-6}$ which is very similar and on the same order of magnitude of the value $\alpha_{1/f} \sim 10^{-7} - 10^{-6}$ measured by the recent experiments in [31] for Sub-ohmic 1/f noise coming from two-level fluctuators, the predicted values of T_1 match our data, meaning our T_1's are consistent with this type of noise. This suggests that our qubit 4 on the cross-cavity chip is currently subject to and limited by 1/f noise from these two-level fluctuators, and not by an Ohmic bath. This is somewhat unexpected because 1/f noise is usually only considered at low-frequencies. Apparently the tale of the 1/f source may well reach our higher qubit frequencies and cause the relaxation.

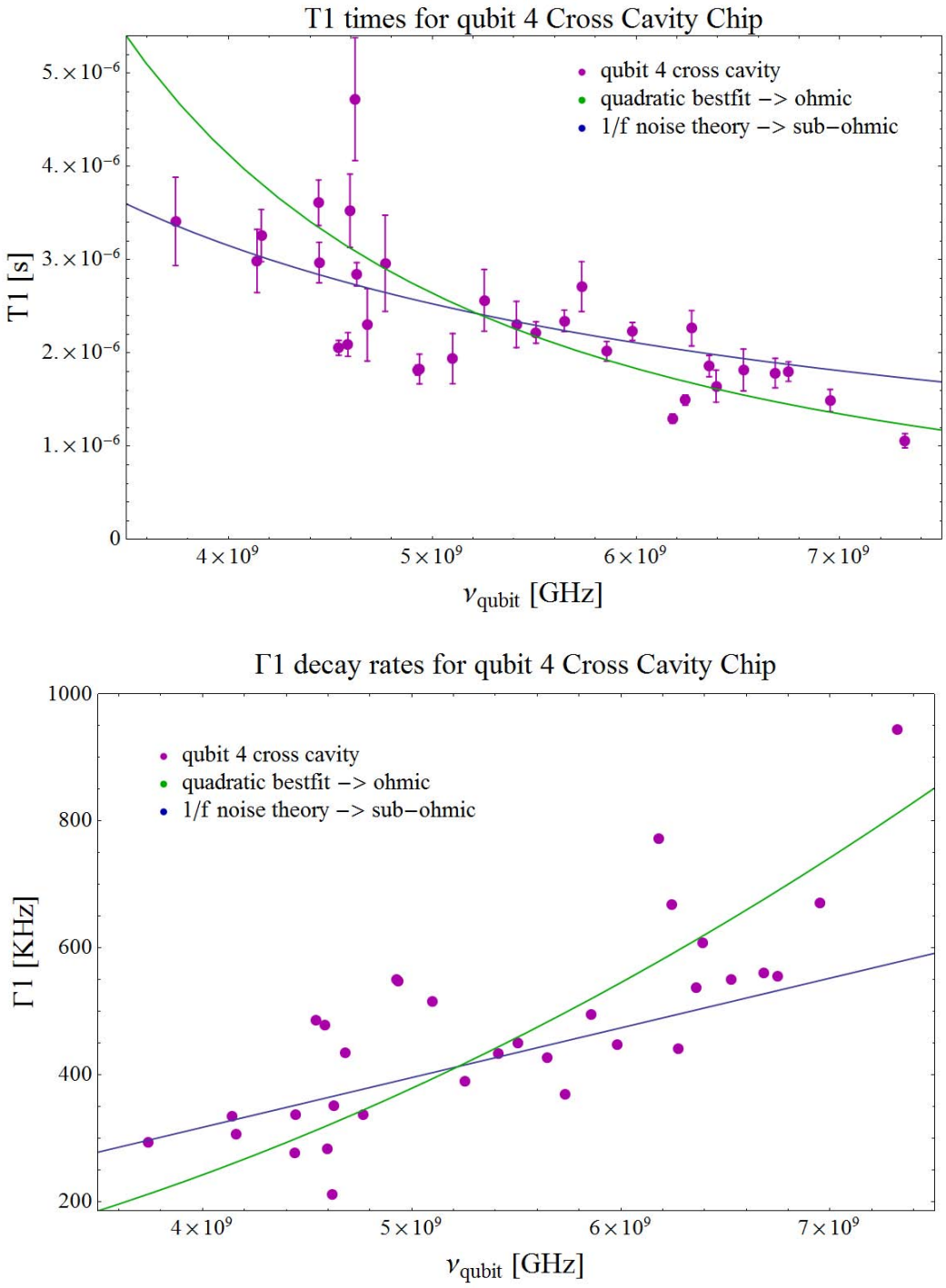

Figure 6.6: The T_1 (top) and Γ_1 (bottome) results from qubit 4 fitted to a quadratic data best fit (green line) and fitted to the theoretical model for a 1/f noise bath (blue line).

Chapter 7

Conclusion

7.1 Summary

The first part of this thesis aimed at suppressing external radiation from the dilution refrigerator which presumably generates quasiparticles tunneling onto the island of the Cooper Pair Box, thereby causing decoherence of the transmon. We embedded the entire 8-port sampleholder into a magnetically loaded, microwave absorptive medium. Two molds were used to form this two-part box that one can open to extract and replace the sample with its printed circuit board. This Eccosorb box was fabricated twice, the first time with the rubber Eccosorb CRS-124 which eventually cracked open in the DR, and the second time with the rigid Eccosorb CR-124.

For both boxes, we then measured T_1 and T_2 times at various qubit frequencies ranging from $\sim$ 4 to 7 GHz. This was done for three different cases: prior to the embedding, then with the broken Eccosorb, and finally with the rigid one. The results showed that the embedding did not lead to an improvement in the relaxation and dephasing times of our three transmon qubits. However, qubit A and B measurements allowed to observe a dependance of $\Gamma_1 (= 1/T_1)$, and an inverse dependance of Γ_2, on the qubit frequency. The data range is though not large enough to conclude if the dependency is linear of quadratic.

In the second part of this thesis, we measured T_1 and T_2 sweeping the qubit 4 frequency of a new sample comprising 4 qubits and 3 cross resonators. The new transmon had a slightly increased gap between its finger capacitors. The results demonstrated a clear improvement by a factor of ~ 3 times for the relaxation time, reaching a maximum value of $T_1 = 4.7$ μs at $\nu_{qb4} = 4.6$ GHz, and by a factor of ~ 2 times for the dephasing time, reaching a maximum value of $T_2 = 996$ ns at $\nu_{qb4} = 7$ GHz. This was attributed to the fact that larger gaps lead to weaker electric fields and therefore less dissipative charge noise.

Furthermore, these results showed again the same frequency dependence as for the first sample. Since the improvement in coherence is related to the strength of electric fields in the qubit, the theoretical relaxation rate for a charge noise bath coupled to the transmon was calculated. The linear or quadratic dependency of the decay rate on qubit frequency in our data led us to conclude that the noise bath should be either ohmic or sub-ohmic. We compared our data to a model describing sub-ohmic 1/f noise, which is known from recent experiments to be present in superconducting Josephson devices, and is due to two-level fluctuators. Fitting this model to our data gave us similar values for the dissipation strength parameter $\alpha_{1/f}$ as the one measured in these recent experiments. This gave us a hint that it could be 1/f noise from two-level fluctuators that is currently limiting the relaxation time of our qubits.

7.2 Outline

The transmon is an example of a mesoscopic system composed of millions of atoms, but still displaying full quantum behavior such as coherence and entanglement. Also, recent experiments have shown that bigger is better, i.e. that a bigger Cooper Pair Box island improves the coherence times. But just how big can we make a transmon such that it still allows for coherence? The next step for our qubits is to fabricate gradually larger transmons and measure improvements in T_1 and T_2. Fig. 7.1 shows the design of such a bigger transmon which will be fabricated next in the QuDev Group.

From our measurement results we saw that the data range for the qubit frequency sweeps is mostly too limited in order to determine the exact dependency of T_1. Measuring greater ranges would allow to observe if it is linear of quadratic, which in turn would give a more precise hint as to what type of noise is limiting the relaxation times in our qubits.

Even though the Eccosorb embedding did not result in T_1 or T_2 improvements for our current transmons, it is not excluded that at some later stage, when the current limiting mechanisms will have been overcome, the generation of quasiparticles suddenly starts to take effect, thereby reviving the use of Eccosorb.

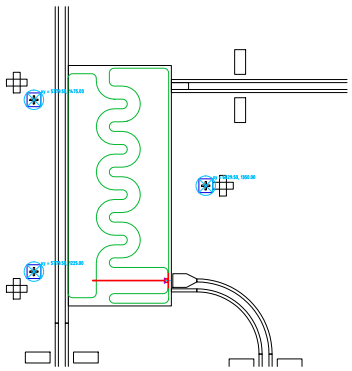

Figure 7.1: New design for a larger transmon, presumably and hopefully having higher coherence times due to the increase in size.

Remerciements

I would like to thank Prof. Dr. Andreas Wallraff for offering me the opportunity to conduct my Master Thesis in the QuDev Group at ETH Zurich. As a theoretical physics student in the masters it was extremely difficult for me to imagine which field of research would interest me the most. I chose randomly. It is amazing that chance brought me to a field, namely that of superconducting qubits, which finally captivated my interest at such a degree that I have now decided to pursue graduate research in this field for a PhD at the University of Oxford.

My greatest thanks goes to Dr. Arkady Fedorov, my supervisor, who was always willing to explain and help me with the difficulties in the project. I can say that most of my current experimental knowledge on superconducting qubits stems from him. I had great pleasure working together with him, and also enjoyed the many interesting discussions on Russian politics and international relations. I wish him and his family all the best for his new Professorship at the University of Queensland in Australia.

Furthermore, thanks to Matthias Baur, Lars Steffen, Markus Oppliger and Simon Berger for their practical support with the experimental setup and software, as well as Janis Luetolf for fabricating the molds. Thanks to Arjan Van Loo, Marek Pechal, Yulin Liu and Kristinn Juliusson for the many discussions on physics and the world. En outre, je remercie Julian Cancino, Romain M*ü*ller, et Vincent Beaud de m'avoir aid*é à r*éussir mes examens de première. Et je remercie surtout mes super parents Bruno et Claudia ainsi que ma copine Karen de m'avoir toujours support*é* et pouss*é* pendants mes *acutee*tudes, sans eux je ne serais pas arriv*é* si loin.

Finally, I would like give a particular thanks to all my special friends and real shizzls of Zurich for the amaaazing times we had together in the VSETH Vorstand, organising the Challenge'11 ETHZ-EPFL, organising the ESF and Sonafe, and all the other random and `goil` shizzlation we experienced together. An Energy & Passion shoutout for Andri Bargetzi, Roman Saratz, Claudio Paganini, Barbara Gerig, Patrick Aubry, Janick Griner, Remo Gisi, Susanne Tobler, Andi Ritter, and Martin Sack. The good times are short, but the memories stay forever. I will miss you guys in Oxford.

Bibliography

[1] Peter W. Shor. Polynomial-time algorithms for prime factorization and discrete logarithms on a quantum computer. *SIAM Journal on Scientific and Statistical Computing*, 26:1484, 1997.

[2] Lov K. Grover. A fast quantum mechanical algorithm for database search. In *Proceedings of the twenty-eighth annual ACM symposium on Theory of computing*, pages 212–219, Philadelphia, Pennsylvania, United States, 1996. ACM.

[3] R. P. Feynman. Simulating physics with computers. *International Journal of Theoretical Physics*, 21(6):467–488, June 1982.

[4] Daniel Loss and David P. DiVincenzo. Quantum computation with quantum dots. *Phys. Rev. A*, 57(1):120–, January 1998.

[5] N. Gershenfeld and I. Chuang. Bulk spin resonance quantum computation. *Science*, 275:350–356, 1997.

[6] David G. Cory, Amr F. Fahmy, and Timothy F. Havel. Ensemble quantum computing by NMR spectroscopy. *Proceedings of the National Academy of Sciences*, 94(5):1634–1639, March 1997.

[7] Isaac L. Chuang and Yoshihisa Yamamoto. Simple quantum computer. *Phys. Rev. A*, 1995.

[8] J. I. Cirac and P. Zoller. Quantum computations with cold trapped ions. *Phys. Rev. Lett.*, 74:4091–4094, May 1995.

[9] A. Blais, R.-S. Huang, A. Wallraff, S. M. Girvin, and R. J. Schoelkopf. Cavity quantum electrodynamics for superconducting electrical circuits: An architecture for quantum computation. *Phys. Rev. A*, 69(6):062320, June 2004.

[10] Lars Steffen. Local qubit control in circuit quantum electrodynamics. Master's thesis, Laboratory of solid state physics, ETH Zurich, 2008.

[11] Yuriy Makhlin, Gerd Schön, and Alexander Shnirman. Quantum-state engineering with Josephson-junction devices. *Rev. Mod. Phys.*, 73(2):357–400, May 2001.

[12] B. D. Josephson. Possible new effects in superconductive tunnelling. *Physics Letters*, 1(7):251–253, July 1962.

[13] M. Tinkham. *Introduction to Superconductivity*. McGraw-Hill International Editions, 1996.

[14] Matteo Mariantoni. *New Trends in Superconducting Circuit Quantum Electrodynamics: Two Amplifiers, Two Resonators, and Two Photons*. Shaker Verlag, 2010.

[15] Denis Vion. Josephson quantum bits based on a cooper parir box. 2003.

[16] D. I. Schuster. *Circuit Quantum Electrodynamics*. PhD thesis, Yale University, 2007.

[17] Jens Koch, Terri M. Yu, Jay Gambetta, A. A. Houck, D. I. Schuster, J. Majer, Alexandre Blais, M. H. Devoret, S. M. Girvin, and R. J. Schoelkopf. Charge-insensitive qubit design derived from the Cooper pair box. *Phys. Rev. A*, 76(4):042319, 2007.

[18] G. Ithier, E. Collin, P. Joyez, P. J. Meeson, D. Vion, D. Esteve, F. Chiarello, A. Shnirman, Y. Makhlin, J. Schriefl, and G. Schön. Decoherence in a superconducting quantum bit circuit. *Phys. Rev. B*, 72:134519, 2005.

[19] Simon Berger. Observation of a berry's phase in a transmon qubit. Master's thesis, Laboratory of solid state physics, ETH Zurich, 2010.

[20] A. Wallraff, D. I. Schuster, A. Blais, L. Frunzio, R.-S. Huang, J. Majer, S. Kumar, S. M. Girvin, and R. J. Schoelkopf. Strong coupling of a single photon to a superconducting qubit using circuit quantum electrodynamics. *Nature*, 431:162–167, 2004.

[21] Johannes Fink. Single qubit control and observation of Berry's phase in a superconducting quantum circuit. Master's thesis, Universität Wien, 2007.

[22] M. Göppl. *Engineering Quantum Electronic Chips - Realization and Characterization of Circuit Quantum Electrodynamics Systems*. PhD thesis, ETH Zurich, 2009.

[23] M. Göppl, A. Fragner, M. Baur, R. Bianchetti, S. Filipp, J. M. Fink, P. J. Leek, G. Puebla, L. Steffen, and A. Wallraff. Coplanar waveguide resonators for circuit quantum electrodynamics. *J. Appl. Phys.*, 104:113904, 2008.

[24] M. Baur, A. Fedorov, L. Steffen, S. Filipp, M. P. da Silva, and A. Wallraff. Benchmarking a quantum teleportation protocol in superconducting circuits using tomography and an entanglement witness. *Phys. Rev. Lett.*, 108:040502, Jan 2012.

[25] A. Fedorov, L. Steffen, M. Baur, M. P. da Silva, and A. Wallraff. Implementation of a toffoli gate with superconducting circuits. *Nature*, 481(7380):170–172, jan 2012.

[26] F. Pobell. *Matter and methods at low temperatures*. Springer, 2nd edition, 1995.

[27] Matthias Baur. *Realizing quantum gates and algorithms with three superconducting qubits*. PhD thesis, ETH Zurich, 2012.

[28] Christian Lang. Read-out strategies for multi-qubit states in circuit quantum electrodynamics. Diploma thesis, LMU Munich, 2009.

[29] Antonio D. Córcoles, Jerry M. Chow, Jay M. Gambetta, Chad Rigetti, J. R. Rozen, George A. Keefe, Mary Beth Rothwell, Mark B. Ketchen, and M. Steffen. Protecting superconducting qubits from radiation. *Appl. Phys. Lett.*, 99(18):181906, 2011.

[30] J. Leppäkangas and Michael Marthaler. Fragility of flux qubits against quasiparticle tunneling. *Phys. Rev. B*, 85:144503, 2012.

[31] Alexander Shnirman. Noise and decoherence in quantum two-level systems. 2002.

[32] Y. Nakamura, Yu. A. Pashkin, T. Yamamoto, and J. S. Tsai. Charge echo in a Cooper-pair box. *Phys. Rev. Lett.*, 88(4):047901, Jan 2002.